A Theoretical Study of Calcium Microdomains in Turtle Hair Cells

Yuh-Cherng Wu, Tom Tucker, and Robert Fettiplace
Department of Neurophysiology, University of Wisconsin Medical School, Madison, Wisconsin 53706 USA

ABSTRACT Confocal imaging has revealed microdomains of intracellular free Ca^{2+} in turtle hair cells evoked by depolarizing pulses and has delineated factors affecting the growth and dissipation of such domains. However, imaging experiments have limited spatial and temporal resolution. To extend the range of the results we have developed a three-dimensional model of Ca^{2+} diffusion in a cylindrical hair cell, allowing part of the Ca^{2+} influx to occur over a small circular region (radius 0.125–1.0 μm) representing a high-density array of voltage-dependent channels. The model incorporated experimental information about the number of channels, the fixed and mobile Ca^{2+} buffers, and the Ca^{2+} extrusion mechanism. A feature of the calculations was the use of a variable grid size depending on the proximity to the Ca^{2+} channel cluster. The results agreed qualitatively with experimental data on the localization of the Ca^{2+} transients, although the experimental responses were smaller and slower, which is most likely due to temporal and spatial averaging in the imaging. The model made predictions about 1) the optimal Ca^{2+} channel number and density within a cluster, 2) the conditions to ensure independence of neighboring clusters, and 3) the influence of the Ca^{2+} buffers on the kinetics and localization of the microdomains. We suggest that an increase in the mobile Ca^{2+} buffer concentration in high-frequency hair cells (which possess a larger number of release sites) would allow lower amplitude and faster Ca^{2+} responses and promote functional independence of the sites.

INTRODUCTION

Intracellular free calcium (Ca^{2+}) regulates multiple processes in hair cell transduction, from modulation of the adaptive state of the mechanoelectrical transducer channels in the apically placed hair bundle to the rapid release of chemical transmitter at afferent synaptic junctions on the basolateral membrane (Fettiplace, 1992; Lenzi and Roberts, 1994). These various functions are spatially separated, and to appreciate their coordination, a knowledge is required of the factors determining the diffusion of Ca^{2+} through the cytoplasm after influx via membrane channels. The problem has been addressed experimentally by monitoring Ca^{2+} signals by confocal imaging of hair cells filled with a fluorescent Ca^{2+} indicator (Tucker and Fettiplace, 1995). These imaging experiments have revealed hotspots, microdomains of high Ca^{2+} concentration, which appear during depolarizations large enough to activate voltage-dependent Ca^{2+} channels. The hotspots are consistent with Ca^{2+} entry occurring at a small number of sites on the basolateral membrane of the hair cell, suggesting that the Ca^{2+} channels may be arranged in clusters. Such channel aggregates have been previously postulated in frog saccular hair cells on the basis of loose-patch recordings, and it has been suggested that they are localized to the synaptic release sites on the dendrites of VIIIth nerve fibers (Roberts et al., 1990). An important question relates to whether the properties of the channel aggregates, their size and spacing, affect the spread of the Ca^{2+} signals. What are the conditions for each hotspot to behave independently of the others? How are the Ca^{2+} dynamics at each channel cluster influenced by the local Ca^{2+} handling mechanisms, the buffers and pumps? These questions are difficult to answer solely on the basis of experiments. However, they are important for understanding Ca^{2+} signaling in many neurons and are particularly pertinent to control of transmitter release at presynaptic nerve terminals (Heidelberger et al., 1994).

A number of studies have modeled Ca^{2+} diffusion at the nerve terminal with the aim of predicting the rapid time course of Ca^{2+}-dependent transmitter release (e.g., Chad and Eckert, 1984; Simon and Llinás, 1985; Yamada and Zucker, 1992). These studies used numerical solutions of the diffusion equation for small compartments a few nanometers in size. They led to the idea of microdomains of Ca^{2+} reaching 100 μM or more, which rapidly develop at the mouth of open Ca^{2+} channels and which collapse within a few milliseconds of channel closure. Support for such domains of high Ca^{2+} concentration has been derived from imaging experiments (Llinás et al., 1992, 1995; Petrozzino et al., 1995; Tucker and Fettiplace, 1995) although in general the experimental techniques have more limited spatial resolution than the simulations. Another class of model has been developed to define the role of Ca^{2+} buffers (Sala and Hernández-Cruz, 1990; Nowycky and Pinter, 1993; Roberts, 1994; Smith et al., 1996). Such models, in which a spherical cell is represented as concentric shells or where $[Ca^{2+}]$ diffuses from a point source into a hemispherical space, have emphasized the importance of the buffers in shaping the Ca^{2+} transients and, for the diffusible buffer, in accelerating Ca^{2+} equilibration throughout the cell. However, they are limited in being unable to represent lateral heterogeneity across the cell surface as is required for nonuniform distribution of Ca^{2+} channels. In the present study we have attempted to blend the two types of model by applying a three-dimensional reconstruction with a rela-

Received for publication 1 May 1996 and in final form 23 August 1996.
Address reprint requests to Dr. Robert Fettiplace, 273 Medical Sciences Building, 1300 University Avenue, Madison WI, 53706. Tel.: 608-262-9320; Fax: 608-265-3500; E-mail: fettiplace@neurophys.wisc.edu.

0006-3495/96/11/2256/20 $2.00

tively small grid size to Ca^{2+} homeostasis across the entire hair cell. The aim was first to compare the simulations with the imaging experiments of Tucker and Fettiplace (1995) and then use the model to extend the spatial and temporal resolution over those achievable experimentally.

THEORY

Geometrical considerations of the model hair cell

A three-dimensional compartment model was constructed to simulate the spreading of free Ca^{2+} ions and various buffers within the cytoplasmic space for an isolated turtle hair cell. Based on the cylindrical shape of the hair cell, the space is compartmentalized in cylindrical coordinates (r, θ, and z; Fig. 1). The cell dimensions are radius $a = 5$ μm and length $l = 30$ μm in the r and z coordinates respectively. The positive directions in the θ and z coordinates are assigned to be clockwise and downward. The Ca^{2+} channels are located only on the bottom half of the cell membrane whereas the fixed and diffusible buffers are distributed uniformly within the entire cytoplasmic space in the initial steady state. The free Ca^{2+} ions, free diffusible buffers, and Ca^{2+}-bound diffusible buffers are allowed to spread throughout the cytoplasm with various diffusion coefficients. Although evidence suggests that a CaATPase in an intracellular compartment contributes to the Ca^{2+} removal (Tucker and Fettiplace, 1995), such a mechanism is not incorporated into the model due to insufficient information about its parameters.

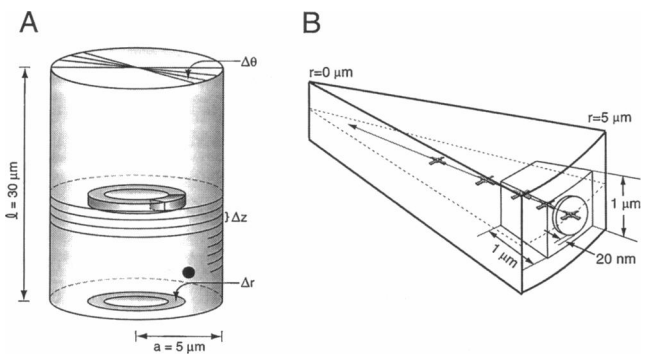

FIGURE 1 (*A*) Computations were performed on a cylindrical hair cell with a coordinate system (r,θ,z). For simplicity, the hair bundle, which would normally be at the top of the cell ($z = 0$), was not included in the model. The hair cell has a length of 30 μm and a radius of 5 μm, which are average values based on measurements of isolated turtle hair cells. The center of the hotspot (black spot) was located approximately one-sixth of the distance from the bottom of the cell ($r = 5$ μm; $z = 24.5$ μm). (*B*) Segment of the cell indicating the values of Ca^{2+} concentration computed in the vicinity of the hotspot: $[Ca^{2+}]_{xnm}$ (where $x = 10$, 80, 450, 1400, and 2750), denoted by five crosses, values along the radius at distances of 10, 80, 450, 1400, and 2750 nm from the center of the hotspot; $[Ca^{2+}]_{avghs}$, the average value for a 20-nm cytoplasmic slab beneath the hotspot; and $[Ca^{2+}]_{bot}$, the average value in a block of cytoplasm of volume ~ 1 μm^3 beneath the hotspot. The block was defined by $r = 4$–5 μm, $\Delta z = 1$ μm, and $\Delta\theta = 12°$; a second block (not shown) for $[Ca^{2+}]_{bot2}$ was defined by $r = 3.5$–4.5 μm, $\Delta z = 1$ μm, and $\Delta\theta = 12°$.

Diffusion equations

The diffusion component in cylindrical coordinates can be described as follows:

$$\left[\frac{\partial u}{\partial t}\right]_{\text{diffusion}} = D_u \nabla^2 u$$

$$= D_u\left\{\frac{1}{r}\frac{\partial}{\partial r}\left(r\cdot\frac{\partial u}{\partial r}\right) + \frac{1}{r^2}\frac{\partial^2 u}{\partial \theta^2} + \frac{\partial^2 u}{\partial z^2}\right\}, \quad (1)$$

where u can be concentrations of free Ca^{2+} ions, Ca^{2+}-bound or Ca^{2+}-free diffusible buffers, and D_u is the diffusion coefficient of the substance u.

Voltage-dependent Ca^{2+} channel

The description of the voltage-dependent Ca^{2+} channel has been justified elsewhere (Wu et al., 1995), but for convenience, the main equations are reproduced here. Ca^{2+} currents in turtle hair cells can be fit by an m^2 relation (Art and Fettiplace, 1987) consistent with the following kinetic scheme for closed (C) and open (O) states:

$$\begin{bmatrix} \beta_m \\ C \rightleftharpoons O \\ \alpha_m \end{bmatrix}^2, \quad (2)$$

with a gating probability, O_m, given by the differential equation

$$\frac{dO_m}{dt} = \beta_m(1 - O_m) - \alpha_m O_m, \quad (3)$$

and rate constants for opening (β_m in s^{-1}) and closing (α_m in s^{-1}) that depend on membrane potential V in mV:

$$\alpha_m = 5.5e^{-V/8.0} + 765, \quad (4)$$

$$\beta_m = 1.23 \times 10^5 e^{V/6.2} + 1410. \quad (5)$$

These values were derived from fits to experimental records giving a half-activation for the conductance at -30 mV, a slope factor of 8.0 mV, and an activation time constant of approximately 0.3 ms at -50 mV. The probability of opening of the Ca^{2+} channel, p_{Ca}, is then

$$P_{Ca} = (O_m)^2. \quad (6)$$

The single-Ca^{2+}-channel current, i_{Ca}, was calculated from the constant field equation

$$i_{Ca} = \frac{P'\varepsilon(e^{-\varepsilon}[Ca^{2+}]_o/[Ca^{2+}]_i - 1)}{e^{-\varepsilon} - 1}, \quad (7)$$

where $n = 2FV/RT \approx 0.08V$. The values of the constant P' in pA and the ratio $[Ca^{2+}]_o/[Ca^{2+}]_i$ were evaluated as described previously (Wu et al., 1995) but with the exception that the single-channel current was increased. This change was made for comparison with experiments (Tucker

and Fettiplace, 1995) in which the $[Ca^{2+}]_o$ was raised to 5 mM; i_{Ca} becomes, in pA,

$$i_{Ca} = \frac{9.88 \times 10^{-5}\varepsilon(2981e^{-\varepsilon} - 1)}{e^{-\varepsilon} - 1}. \quad (8)$$

The averaged single Ca^{2+} current, $\bar{i}_{Ca}$, is

$$\bar{i}_{Ca} = i_{Ca}p_{Ca} \quad (9)$$

and has a value of approximately 0.46 pA at −20 mV.

Ca^{2+} fluxes

The rate of change of free Ca^{2+} concentration due to the opening or closing of Ca^{2+} channels is defined as

$$\left[\frac{\partial[Ca^{2+}]}{\partial t}\right]_{influx} = \frac{-n_{Ca}(r, \theta, z)\bar{i}_{Ca}(t)}{2FV_c}, \quad (10)$$

where $\bar{i}_{Ca}(t)$ is the averaged current of a single Ca^{2+} channel as defined in Eq. 9, F is Faraday's constant, $n_{Ca}(r, \theta, z)$ is the total number of Ca^{2+} channels in a compartment located at (r, θ, z), and V_c is the volume of that specific compartment.

Ca^{2+} extrusion and leakage

The CaATPase pumps distributed at the bottom half of the cell membrane are modeled according to Michaelis-Menten kinetics (Sala and Hernández-Cruz, 1990; Nowycky and Pinter, 1993). An inward Ca^{2+} leakage is provided in opposition to the Ca^{2+} extrusion mechanism to maintain the initial steady state before applying the voltage steps (Sala and Hernández-Cruz, 1990). The combination of Ca^{2+} extrusion and leakage then can be defined as

$$\left[\frac{\partial[Ca^{2+}]}{\partial t}\right]_{ex+leak} = \frac{\nu_{max}A(r, \theta, z)}{V_c} \cdot \left(\frac{[Ca^{2+}]_o}{[Ca^{2+}]_o + K_m} - \frac{[Ca^{2+}]}{[Ca^{2+}] + K_m}\right). \quad (11)$$

where $[Ca^{2+}]_o$ is the initial steady-state concentration, ν_{max} and K_m are the maximal velocity of transport and the half-maximal activation for the CaATPase pumps, and $A(r, \theta, z)$ is the effective pumping area of a compartment (r, θ, z).

Cluster of Ca^{2+} channels

The cluster of Ca^{2+} channels, referred to as the hotspot, is modeled by assuming that the cluster is sufficiently small to be treated as a circular area with radius r_h located at the membrane. The center of the cluster has coordinates of (r_c, θ_c, z_c), where $r_c = a$ for the cluster located at the cell membrane. The location of the cluster can then be approximated if the coordinate (a, θ, z) satisfy the following criterion:

$$(z - z_c)^2 + (a\theta - a\theta_c)^2 \le r_h^2, \quad (12)$$

which can be rearranged as

$$-\frac{1}{a}\sqrt{r_h^2 - (z - z_c)^2} + \theta_c \le \theta \le \frac{1}{a}\sqrt{r_h^2 - (z - z_c)^2} + \theta_c,$$

and

$$z_c - r_h \le z \le z_c + r_h. \quad (13)$$

Note that Eq. 13 assumes that the cluster is located at the position where $z_c + r_h < l$, $z_c - r_h > 0$, and θ is continuous, i.e., not on the boundary of 0 and 2π.

Ca^{2+} channel density

The mapping between the total number of Ca^{2+} channels, N_{Ca}, and the resonant frequency has been derived from experimental observation (Art et al., 1993, Wu et al., 1995). The number of Ca^{2+} channels, N_{Ca}^h, in a single hotspot for a hair cell tuned in the middle frequency range, i.e., 150–300 Hz, can be estimated from the Ca^{2+} imaging study (Tucker and Fettiplace, 1995). The Ca^{2+} channel density within a hotspot can then be expressed in terms of the radius of that hotspot:

$$\rho_{Ca}^h = \frac{N_{Ca}^h}{\pi \cdot r_h^2}. \quad (14)$$

If the value of r_h is assigned, the uniform Ca^{2+} channel density for those located outside the hotspot can be determined as

$$\rho_{Ca}^u = \frac{N_{Ca} - n_h\rho_{Ca}^h\pi r_h^2}{\pi(a^2 + 2a\ell d_{Ca} - n_h r_h^2)}, \quad (15)$$

where n_h is the total number of hotspots and $d_{Ca} = 0.5$ is the proportion of membrane along the z direction where the Ca^{2+} channels are distributed.

Fixed buffers

First-order kinetics are assumed for the binding and unbinding of the fixed buffer:

$$Ca^{2+} + B_F \underset{k_F^-}{\overset{k_F^+}{\rightleftharpoons}} CaB_F, \quad (16)$$

where B_F and CaB_F represent the Ca^{2+}-free and Ca^{2+}-bound fixed buffers and k_F^+ and k_F^- are the binding and unbinding rate constants. The dissociation constant k_F^d is equal to k_F^-/k_F^+. From Eq. 16, the rate of change of free

$[Ca^{2+}]$ by the fixed buffer is given as:

$$\left[\frac{\partial[Ca^{2+}]}{\partial t}\right]_{fixed} = k_F^d k_F^+([B_F^T] - [B_F]) - k_F^+[Ca^{2+}][B_F], \quad (17)$$

where $[B_F^T]$ is the total concentration of B_F. The rates of change of free and Ca^{2+}-bound buffers can also be related to Eq. 17:

$$\left[\frac{d[B_F]}{dt}\right] = -\left[\frac{d[CaB_F]}{dt}\right] = \left[\frac{\partial[Ca^{2+}]}{\partial t}\right]_{fixed}. \quad (18)$$

As the fixed buffer is assumed to be uniformly distributed throughout the whole cytoplasmic space, $[B_F^T]$ is a constant for all compartments. Experimental data gleaned from use of the fluorescent indicator Calcium Green 5N in hair cells suggests that, in the $[Ca^{2+}]$ range above 1 μM, only approximately 0.5% of the Ca^{2+} entering remained free (Tucker and Fettiplace, 1995). The ratio $[B_F^T]/k_F^d$ can therefore be determined as approximately 200.

Diffusible buffers

The kinetic scheme of the diffusible buffer is assumed the same as the fixed buffer:

$$Ca^{2+} + B_D \underset{k_D^-}{\overset{k_D^+}{\rightleftharpoons}} CaB_D, \quad (19)$$

where B_D and CaB_D represent the Ca^{2+}-free and Ca^{2+}-bound diffusible buffers, and k_D^+ and k_D^- are the binding and unbinding rate constants. The dissociation constant k_D^d is equal to k_D^-/k_D^+. By considering the relative molecular weights of a Ca^{2+} ion and the free diffusible buffers, e.g., EGTA or BAPTA in this study, the diffusion coefficients of Ca^{2+}-free and Ca^{2+}-bound diffusible buffers could be assumed the same. If the B_D and CaB_D are treated as a single species, the net exchange of $[B_D]$ and $[CaB_D]$ between one compartment and its surrounding compartments becomes zero, i.e., the total buffer concentration is remained fixed, and thus the spatial distribution of total buffer is unaffected by $[Ca^{2+}]$ (Neher, 1986; Roberts, 1994). Then, the rate of change of free $[Ca^{2+}]$ produced by the diffusible buffer can be defined, as for the fixed buffer, as

$$\left[\frac{\partial[Ca^{2+}]}{\partial t}\right]_{mobile} = k_D^d k_D^+([B_D^T] - [B_D]) - k_D^+[Ca^{2+}][B_D], \quad (20)$$

where $[B_D^T]$ is the total concentration of B_D. The rate of changes of Ca^{2+}-free and Ca^{2+}-bound buffers can also be related to Eq. 20:

$$\left[\frac{\partial[B_D]}{\partial t}\right] = -\left[\frac{\partial[CaB_D]}{\partial t}\right] = \left[\frac{\partial[Ca^{2+}]}{\partial t}\right]_{mobile} + D_B\nabla^2[B_D], \quad (21)$$

where $\nabla^2[B_D]$ is the differential operator defined in Eq. 1.

Integration

Two ordinary and two partial differential equations (ODEs and PDEs) need to be integrated to calculate the spread of free Ca^{2+}. The first ODE is Eq. 3 describing the open probability of Ca^{2+} channels. The other one is Eq. 18 calculating the concentration of free fixed buffer. Both PDEs are related to the diffusion process. The first PDE is Eq. 21, which determines the concentration of Ca^{2+}-free diffusible buffer of each compartment. The second one integrates the various components describing the total rate of change of $[Ca^{2+}]$, which is a summation of Eqs. 1, 10, 11, 17, and 20:

$$\frac{\partial[Ca^{2+}]}{\partial t} = \left[\frac{\partial[Ca^{2+}]}{\partial t}\right]_{diffusion} + \left[\frac{\partial[Ca^{2+}]}{\partial t}\right]_{influx} + \left[\frac{\partial[Ca^{2+}]}{\partial t}\right]_{ex+leak} + \left[\frac{\partial[Ca^{2+}]}{\partial t}\right]_{fixed} + \left[\frac{\partial[Ca^{2+}]}{\partial t}\right]_{mobile}. \quad (22)$$

Numerical methods, finite difference equations, and boundary conditions are given in the Appendix.

RESULTS

Summary of experimental observations

A starting point in the modeling was the Ca^{2+} responses measured in isolated hair cells with Calcium Green 5N (Tucker and Fettiplace, 1995, 1996), a low-affinity calcium dye with $K_D \approx 30$ μM. Although the confocal imaging used in those experiments imposed both spatial and temporal constraints, nevertheless, it was possible to reach conclusions about Ca^{2+} localization at the hotspots. These conclusions, summarized below, were used to set many of the model parameters listed in Table 1.

Hotspot properties

On depolarization of the hair cell to -20 mV, up to six hotspots developed in the basal half of the cell, each expanding from a source less than 1 μm in diameter. The maximal Ca^{2+} current in most cells was 600-1000 pA, and a hotspot contributed approximately 100 pA, estimated from the extinction of a spot by local application of a low-Ca^{2+} solution. From Eqs. 8 and 9, the single-channel current at -20 mV is 0.46 pA and, thus each spot comprises 217 channels. As electron microscopic sections indicate that mid-papillar turtle hair cells (used predominantly in the imaging experiments) contain approximately 15–20 release sites (Sneary, 1988), a hotspot may correspond to several neighboring release sites, each containing approximately 50–100 channels (see Discussion).

The peak Ca^{2+} concentration attained in the hotspot at the end of a 300-ms depolarization was estimated as 85 μM; however, it should be emphasized that this concentration

TABLE 1 Parameter definitions and standard values

Symbol	Definition	Standard (other) values
a	Radius of the cell in r direction	5 μm
ℓ	Length of the cell in z direction	30 μm
ν_{max}	Maximal velocity of transport for CaATPase pumps based on 1960 pumps/μm^2 and 200 ions/pump/s	6.5×10^{-4} μ mmol^{-2}s^{-1}
K_m	Half-maximal Ca^{2+} activation for CaATPase	0.2 μM
$[Ca^{2+}]_o$	Initial steady-state Ca^{2+} concentration	0.1 μM
D_{Ca}	Diffusion coefficient of free Ca^{2+} ions*	400 $\mu m^2 s^{-1}$
r_h	Radius of hotspot	0.5 (0.125, 0.25, 1) μm
(r_c, θ_c, z_c)	Coordinates of center of first hotspot	5 μm, 0°, 24.5 μm
N_{Ca}	Total number of Ca^{2+} channels	2200
N_{Ca}^h	Total number of Ca^{2+} channels in one hotspot	157 (10, 39, 628)
ρ_{Ca}^h	Density of Ca^{2+} channels inside hotspots	200 (50, 800) μm^{-2}
ρ_{Ca}^u	Density of Ca^{2+} channels outside hotspots	3.72 μm^{-2}
k_F^+	Rate constant for Ca^{2+} binding to the fixed buffer	100 $\mu M^{-1}s^{-1}$
k_F^d	Dissociation constant for fixed buffer	20 μM
$[B_F^T]$	Total concentration of fixed buffer	4 (1) mM
k_D^+ BAPTA	Rate constant for Ca^{2+} binding to BAPTA*	500 $\mu M^{-1}s^{-1}$
k_D^+ EGTA	Rate constant for Ca^{2+} binding to EGTA*	9 $\mu M^{-1}s^{-1}$
k_D^+ Calbindin	Rate constant for Ca^{2+} binding to calbindin*	90 $\mu M^{-1}s^{-1}$
$[B_D^T]$ BAPTA	Total concentration of BAPTA	1 (0.1, 2, 5) mM
$[B_D^T]$ Buffer	Total concentration of EGTA or calbindin	1 mM
k_D^d Buffer	Dissociation constant for BAPTA or EGTA*	0.1 μM
k_D^d Calbindin	Dissociation constant for calbindin*	1 μM
D_B Buffer	Diffusion coefficient for BAPTA or EGTA*	200 $\mu m^2 s^{-1}$
D_B Calbindin	Diffusion coefficient for calbindin*	50 (25, 100) $\mu m^2 s^{-1}$

*Dissociation constant, k_D^d, and forward rate constant, k_D^+, for BAPTA and EGTA were approximated from the following literature values: k_D^d, BAPTA, 0.192 μM (Tsien, 1980); k_D^+, 250–650 $\mu M^{-1}s^{-1}$, values for Fura-2, (Jackson et al., 1987); EGTA, k_D^d, 0.09 μM; k_D^+, 9.6 $\mu M^{-1}s^{-1}$ (Neher, 1986). Experimental data for calbindin-28k indicates that it has 3–4 Ca^{2+}-binding sites with an average k_D^d of 0.5 μM (Bredderman and Wasserman, 1974) or one site with k_D^d = 0.001 μM and 2–3 sites of ~10 μM (Gross et al., 1993); the value of k_D^+ for calbindin-28k is assumed as no experimental value is available. Diffusion coefficients were estimated for a medium twice the viscosity of water using the following aqueous values: Ca^{2+}, 790 $\mu m^2 s^{-1}$ (Hille, 1992); BAPTA, EGTA, 500 $\mu m^2 s^{-1}$, value for Fura-2 (Timmerman and Ashley, 1986); 330 $\mu m^2 s^{-1}$, calculated from tetrapentylammonium ion (Tse et al., 1994); calbindin-28k, ~100 $\mu m^2 s^{-1}$, calculated from the Stokes-Einstein relation for a spherical molecule of M_r 28 kDa. Sources of other parameters are given in the text.

was the average value over a 1-μm^2 area using an objective with an axial resolution under confocal conditions of 1.5 μm. The experimental compartment size of volume ~1 μm^3 is likely to underestimate the concentration adjacent to the membrane.

Spread of Ca^{2+} signal

Expansion of the hotspots was quantified by plotting their area against time after depolarization. The area of a hotspot in a given image was determined by constructing a contour around a spot at a fixed Ca^{2+} concentration. The plots were found experimentally to be approximately linear with slopes of ~65 μm^2/s with 1 mM EGTA as the intracellular Ca^{2+} buffer. The slope was decreased to ~10 μm^2/s by recording with intracellular solutions containing high concentration of the Ca^{2+} buffer BAPTA and was increased to ~180 μm^2/s by blocking Ca^{2+} uptake into intracellular compartments. The slope will be influenced both by the apparent diffusion coefficient for Ca^{2+} and by the threshold concentration used in constructing the contours. In all experiments a similar Ca^{2+} threshold, estimated as 14 ± 3 μM, delineated the contour, so the changes observed will largely reflect changes in Ca^{2+} diffusion away from its site of entry.

Ca^{2+} extrusion mechanism

Removal of Ca^{2+} from turtle hair cells mainly involves a CaATPase pump rather than a Na/Ca exchanger, as extrusion can be blocked by low concentrations of intracellular vanadate but is unaffected by substitution of Li^+ or *N*-methylglucamine for extracellular Na^+ (Tucker and Fettiplace, 1995). An estimate of the pumping rate needed to maintain homeostasis can be derived from the fastest stimulus presentation achievable without a long-term rise in intracellular Ca^{2+}. It was possible to deliver depolarizing pulses up to 1000 ms in duration at a rate of 1/60 s without causing the background Ca^{2+} fluorescence to steadily rise (although in practice, a slower rate of 1/90 s was normally employed to give some margin of safety). The Ca^{2+} load produced by a 1-nA current lasting 1000 ms is 5×10^{-15} mol; to completely remove this load in 60 s requires at least 2.5×10^5 CaATPases, each pumping at a maximal rate of 200 ions/s. In fact, the pumping rate will decline as the Ca^{2+} concentration returns to its resting value, which is assumed to be 0.1 μM. The half-maximal Ca^{2+} concentration required to activate the CaATPase was assumed to be 0.2 μM, which is comparable to the values reported for other vertebrate pumps (Schatzmann, 1989; Carafoli, 1991). It should be emphasized that the steady-state Ca^{2+} concentration of 0.1 μM is determined solely by the balance between a Ca^{2+} extrusion rate and an inward leak at −80 mV (Eq. 11). If, therefore, the steady leak were to be increased, for example, by holding the hair cell at −50 mV, there would be a net gain of Ca^{2+} that would eventually overcome the buffering system and cause the free Ca^{2+} to rise catastrophically. To cope with this influx the number of CaATPases in the intact hair cell may be substantially larger than the value estimated above.

In these calculations all of the Ca^{2+} was assumed to leave by crossing the plasma membrane, although in an experimental situation, some will be carried into the recording pipette by exchange of buffer. The time constant τ for

exchange with the pipette can be approximated by $\tau = RV_{cell}/D_B\rho$ (Oliva et al., 1988), where R is the pipette resistance (10 MΩ), V_{cell} is the cell volume (2.4×10^{-9} cm^3), D_B is the diffusion coefficient for a substance like BAPTA (2×10^{-6} cm^2/s), and ρ is resistivity of the filling solution (70 Ωcm). The inferred time constant is 171 s, so in 60 s approximately 30% of the solution will have exchanged.

Cytoplasmic Ca^{2+} buffers

Both fixed and diffusible buffers were incorporated into the model. The properties of the fixed buffer were based on the experimental measurements showing that when the CaATPase mechanism was blocked, the cytoplasm has a residual buffer capacity of approximately 200 for free Ca^{2+} concentrations of 1–10 μM (Tucker and Fettiplace, 1995). This buffer capacity could be achieved with various combinations of buffer concentration and K_D (e.g., 0.4 mM buffer with K_D = 2 μM or 4 mM buffer with K_D = 20 μM). A higher value of K_D was chosen to ensure, in accord with the experiments, that no stimulus saturated the fixed buffer. As the rate constant for binding Ca^{2+} is unknown, a value of 100 $\mu M^{-1}s^{-1}$ was assumed. Diffusible buffers examined in the simulations included EGTA and BAPTA (both of which were used in various concentrations experimentally) and calbindin-28k (Bredderman and Wasserman, 1974; Fullmer and Wasserman, 1987; Gross et al., 1993). The native diffusible buffer, which may be calbindin-28k (Oberholtzer et al., 1988; Roberts, 1994), was found to be equivalent to approximately 1 mM BAPTA in its ability to influence the time course of the slow tail current mediated by a small-conductance Ca^{2+}-activated K^+ channel (Tucker and Fettiplace, 1996). The use of only two species of Ca^{2+} buffer is undoubtedly an oversimplification. The fixed Ca^{2+} buffering in particular is likely to be more complex, with contributions from various organelles like mitochondria and endoplasmic reticulum and cytoplasmic constituents exhibiting multiple binding sites with a range of K_D values (see Discussion).

Magnitude and time course of model Ca^{2+} signals

The changes in free Ca^{2+} throughout the hair cell in response to a 300-ms depolarizing voltage step are depicted in Fig. 2. For this and all subsequent simulations, the depolarization to −20 mV produced a total inward Ca^{2+} current of 1 nA. A series of snapshots of a longitudinal slice through the cell are shown at various stages during and after the depolarization. At early times, Ca^{2+} accumulates beneath the membrane in the basal half of the cell where the Ca^{2+} channels are localized, the free ion concentration rising to ~500 μM at the hotspot. At later times, Ca^{2+} spreads inward from the membrane and eventually diffuses to the top of the cell, where it never exceeds 1 μM. The small change in Ca^{2+} at the top of the cell is valid even for longer depolarizations up to 1000 ms or under conditions of uniform distribution of the CaATPases. It strongly argues, in agreement with the experimental measurements, that Ca^{2+} entering through channels on the basolateral membrane will have a small effect on processes at the top of the cell where the hair bundle and mechanoelectrical transducer channels are located. The similarity of the model with the experimental results can be seen by comparing the frames at 30, 100, and 300 ms in Fig. 2 with the images in Fig. 1 of Tucker and Fettiplace (1995).

For gauging the Ca^{2+} response and comparing it with experimental data, three different measures of the Ca^{2+} concentration in the vicinity of the hotspot were made (see Fig. 1B): 1) $[Ca^{2+}]_{xnm}$, point concentrations along a radius at distances x of 10, 80, 450, 1400, and 2750 nm from the center of the hotspot, 2) the average concentration, $[Ca^{2+}]_{avghs}$, in a 20-nm slab of cytoplasm beneath the hotspot, and 3) the average concentration in a compartment of volume 1 μm^3 positioned directly under the hotspot, $[Ca^{2+}]_{bot}$ (specified by coordinates r = 4–5 μm, $\Delta\theta$ = 12° and z = 24–25 μm). In addition, a fourth concentration, $[Ca^{2+}]_{top}$, was calculated in a 1-μm^3 compartment at the top of the cell (specified by coordinates r = 4–5 μm, $\Delta\theta$ = 12° and z = 4–5 μm). These different measures are illustrated for a 300-ms depolarizing step in Fig. 3. Both the point $[Ca^{2+}]_{10nm}$ and $[Ca^{2+}]_{avghs}$ have comparable time courses and reach a similar concentration of ~500 μM at the end of the pulse. In contrast, $[Ca^{2+}]_{bot}$ beneath the hotspot is delayed and, at the end of the pulse, sees only approximately one-half the concentration of the other two (Fig. 3 *C*). The underestimate of the concentration at the membrane as a result of averaging over a 1-μm^3 volume is even greater if the 1-μm^3 compartment, instead of extending to the membrane of the hotspot, is bounded by a plane 0.5 μm internal to the membrane. This can be seen by comparing $[Ca^{2+}]_{bot}$ and $[Ca^{2+}]_{bot2}$ in Fig. 3 *C*. $[Ca^{2+}]_{bot}$ is the average concentrations in a 1-μm^3 volume bounded radially by r = 4–5 μm and $[Ca^{2+}]_{bot2}$ is the average concentrations in a 1-μm^3 volume bounded radially by r = 3.5–4.5 μm. $[Ca^{2+}]_{bot}$ was intended for comparison with the imaging data where the Ca^{2+} fluorescence is averaged over a volume of at least 1 μm^3. The difference between $[Ca^{2+}]_{avghs}$ and $[Ca^{2+}]_{bot}$ indicates that the imaging results underestimate both the maximal Ca^{2+} concentration and the speed with which the Ca^{2+} changes occur. Moreover, comparison of $[Ca^{2+}]_{bot}$ and $[Ca^{2+}]_{bot2}$ shows that small errors in positioning the confocal plane interior to the membrane could lead to significant errors in measurement of the size and speed of the Ca^{2+} transients.

As the Ca^{2+} signal measured by point $[Ca^{2+}]$ spreads away from the membrane, its concentration is attenuated (Fig. 3 *B*) to less than 10 μM at the center of the cell. However, the Ca^{2+} signal becomes relatively homogeneous after approximately 1 s and everywhere decays with a common time course. This time course is complex and depends partly on the unloading of the diffusible buffer

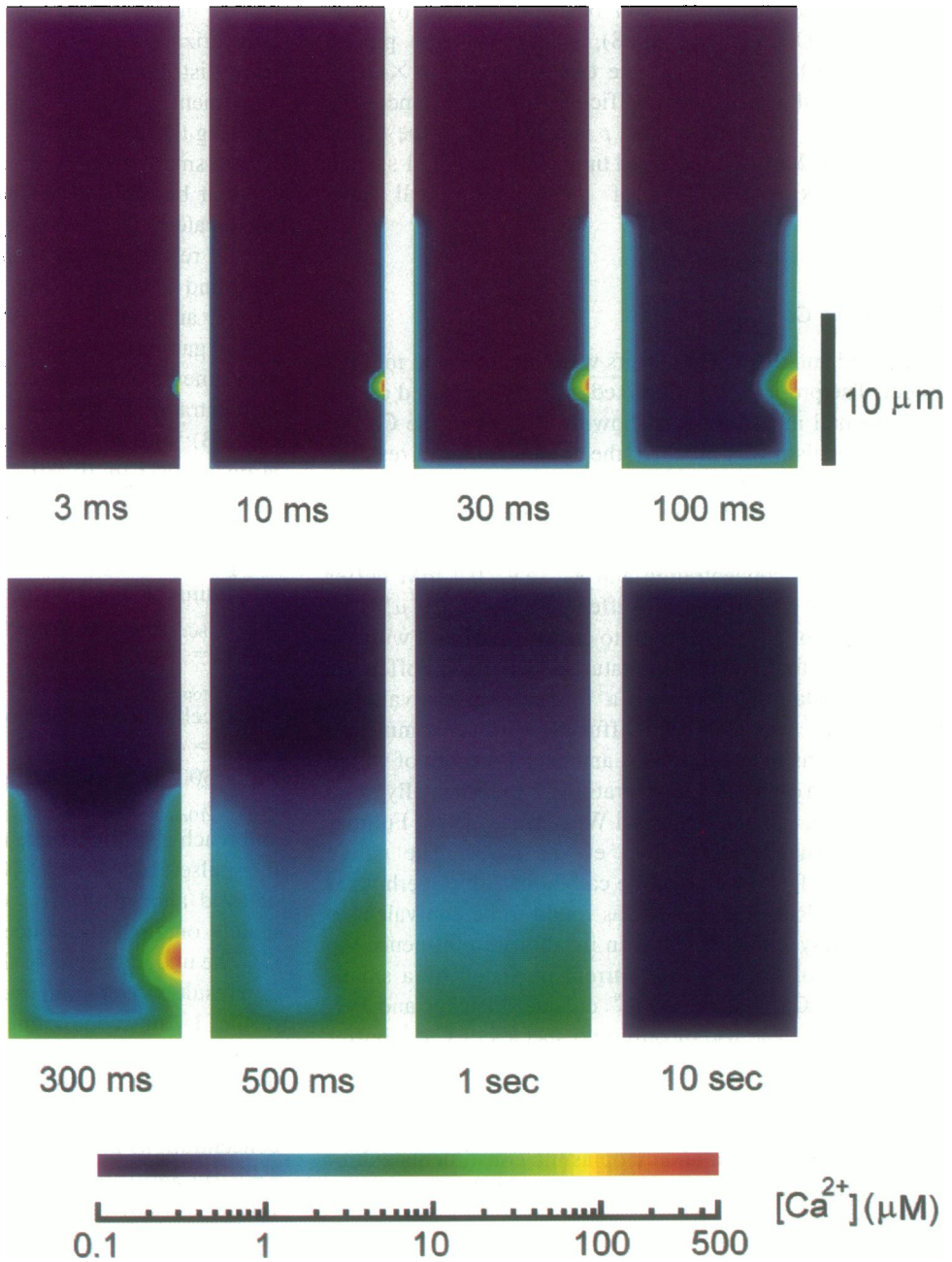

FIGURE 2 Longitudinal slice through the hair cell passing through the center of the hotspot to show the distribution of Ca^{2+} at various times after a 300-ms depolarization from −80 to −20 mV. The pseudocolor scale for the Ca^{2+} concentration is shown logarithmically at the bottom and the times after the depolarization are given next to each section. For the first 30 ms, the rise in Ca^{2+} is confined to the neighborhood of the Ca^{2+} channels, some of which are located at the hotspot and the rest are uniformly distributed over the basal half of the cell. The calculations were performed under standard conditions with 1 mM EGTA diffusible buffer, a hotspot radius of 0.5 μm containing 157 Ca^{2+} channels (density, 200/μm^2), and the remaining 2043 Ca^{2+} channels distributed over the base of the cell.

(Fig. 4) that, with a much higher affinity for Ca^{2+} than the fixed buffer, becomes saturated in the neighborhood of the hotspot. However, although it is tempting to identify a single factor that dominates the time course of decay of the Ca^{2+} signals, most of the processes associated with Ca^{2+} dynamics are likely to make some contribution. Several approaches were used to dissect the parts played by the different factors, the fixed and diffusible buffers and the CaATPase pumps, to the complex time course.

Factors contributing to kinetics

There are both fast and slow phases to the onset and decay of Ca^{2+} around the hotspot (Fig. 3). However, to describe the decay adequately, at least six exponential components were required. For example, in fits to the Ca^{2+} relaxation in Fig. 3, 77% of the total amplitude (extrapolated to end of the pulse) was contributed by components less than 1 ms and 90% less than 14 ms. Other minor components had time constants of ~100 ms, ~800 ms, and ~7 s. This description contrasts with the imaging data, which displayed a Ca^{2+} transient with two major decay time constants of roughly 100 ms and 10 s and where the fast components were absent due to the limited temporal and spatial resolution of the measurements.

A second approach involved decomposition of the Ca^{2+} diffusion equation as shown in Eq. 22 into the sum of components corresponding to the various processes: Ca^{2+}

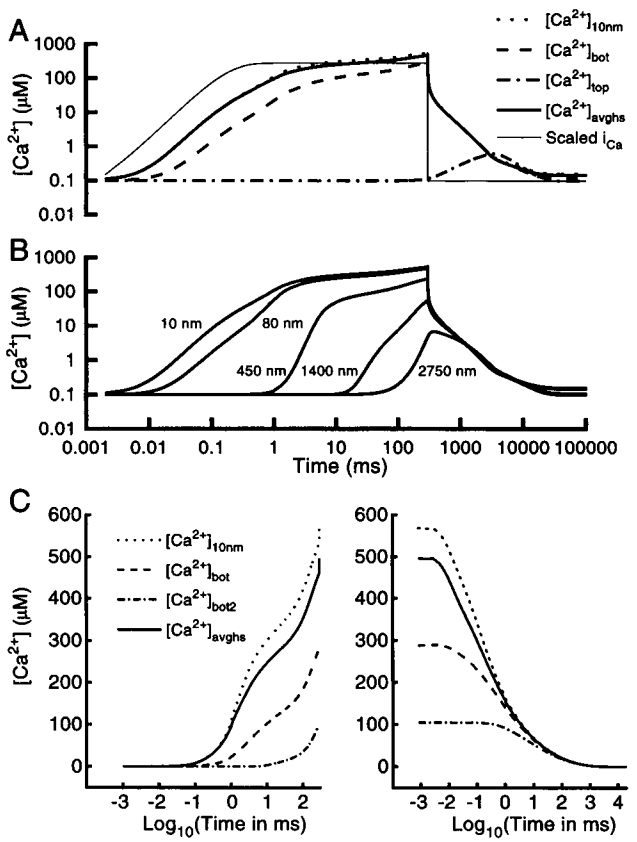

FIGURE 3 (*A*) Changes in $[Ca^{2+}]$ beneath the hotspot in response to a voltage step from −80 to −20 mV. $[Ca^{2+}]_{10\ nm}$, concentration at center of hotspot, 10 nm from the membrane; $[Ca^{2+}]_{avghs}$, average concentration in 20-nm slab beneath the membrane; $[Ca^{2+}]_{bot}$, average concentration in 1 μm^3 of cytoplasm defined (see Fig. 1) by coordinates r = 4–5 μm, z = 24–25 μm, and $\Delta\theta$ = 12°; $[Ca^{2+}]_{top}$, average concentration in 1 μm^3 of cytoplasm beneath membrane at top of cell defined by coordinates r = 4–5 μm, z = 4–5 μm, and $\Delta\theta$ = 12°; i_{Ca}, time course of 1-nA Ca^{2+} current, scaled to overlap concentration changes. (*B*) $[Ca^{2+}]_{xnm}$ changes in calcium concentration in response to a voltage step from −80 to −20 mV at x = 10, 80, 450, 1400, and 2750 nm from the membrane along a radius from the center of the hotspot. (*C*) Comparison of changes in $[Ca^{2+}]$ beneath the hotspot at the onset (*left*) and offset (*right*) of the 300-ms depolarization. Note the $[Ca^{2+}]$ is displayed on a linear scale and the abscissa on the right is measured from the end of the step. Different traces represent the same measurement conditions as in *A* with the addition of $[Ca^{2+}]_{bot2}$, which is the averaged concentration in 1 μm^3 of cytoplasm bounded by a plane 0.5 μm in from the membrane, defined by coordinates r = 3.5–4.5 μm, z = 24–25 μm, and $\Delta\theta$ = 12°. All calculations were performed under standard conditions with 1 mM EGTA diffusible buffer and a hotspot radius of 0.5 μm containing 157 Ca^{2+} channels (density, 200/μm^2).

diffusion, association with fixed and diffusible buffers, and Ca^{2+} leak and extrusion. The relative contribution of each component to the overall Ca^{2+} dynamics could then be observed by plotting $\partial[Ca^{2+}]/\partial t$ against time for each component; a positive derivative indicating a Ca^{2+} increase and a negative derivative signifying Ca^{2+} uptake. Moreover, the relative magnitudes of the different components could be used to identify the dominant effect at a particular time. Three process are important for determining the kinetics after a depolarization: 1) Ca^{2+} diffuses away from the membrane, 2) the fall in Ca^{2+} concentration is slowed by unloading of the fixed buffer, and 3) the diffusible buffer plays a complex role, ferrying the Ca^{2+} away from the hotspot and then, as free buffer, diffusing back to the hotspot from the surrounding regions to bind Ca^{2+} and hence reduce its concentration. The contribution of the diffusible buffer to localization of the Ca^{2+} signal will be reexamined later. One unsurprising conclusion from this type of analysis was that, under standard conditions (see Table 1), the plasma membrane pump makes little contribution to the Ca^{2+} kinetics in the first 500 ms.

Fixed and mobile buffers

Two interrelated factors affect the cell's long-term Ca^{2+} balance. One is the change in free Ca^{2+}; the other is the change in Ca^{2+} bound to the buffers. Fig. 4 shows that the free Ca^{2+} has almost fully recovered after 2 s, and yet the mobile buffer remains bound to Ca^{2+} for much longer. For example, with BAPTA, $[Ca^{2+}]_{10nm}$ has declined to ~0.2% of its peak concentration during the pulse, but ~90% of the buffer is still bound ($[Ca^{2+}]_{10nm}$ declines from 570 μM at the end of the pulse to 1 μM at 2 s after the pulse, whereas the concentration of bound BAPTA decreases from 999.8 μM at the end of the pulse to 909 μM at 2 s after the pulse). The depletion of the buffers after a Ca^{2+} load might be regarded as a Ca^{2+} debt, which must eventually be paid off for the cell to return to its original state. In a dye measurement with a limited signal-to-noise ratio, where the Ca^{2+} concentration is expressed on a linear coordinate, the free Ca^{2+} may appear to have almost completely returned to the baseline, but the cell will still be substantially Ca^{2+} loaded. Free buffer is regenerated ultimately by operation of the CaATPase, and if the pumps are functioning at a reduced capacity (e.g., due to partial block or to reduced ATP supply), the high-affinity buffer will become progressively consumed. This will affect the time course of Ca^{2+} recovery and may explain why block of the extrusion process, although too slow to contribute directly to the kinetics of a single response, nevertheless has an effect on the responses to repetitive presentations.

It is likely that intracellular Ca^{2+} dynamics will be sensitive to the characteristics of the two Ca^{2+} buffers, such as buffer concentration, K_D, and forward rate constant for binding Ca^{2+}. It was not possible to explore all combinations of buffer parameters, but some representative examples were studied. The clearest effect stemmed from raising the concentration of the mobile buffer, which caused a proportional reduction in the maximal Ca^{2+} concentration at the hotspot, severely curtailed the spread of Ca^{2+} beyond the cluster of channels, and accelerated the recovery on Ca^{2+} channel closure. As an illustration, increasing the concentration of BAPTA from 1 to 5 mM reduced the Ca^{2+} beneath the membrane at the hotspot from approximately 500 μM to 100 μM at the end of a 300-ms step; furthermore, after the step, the Ca^{2+} declined to 1% of its value in

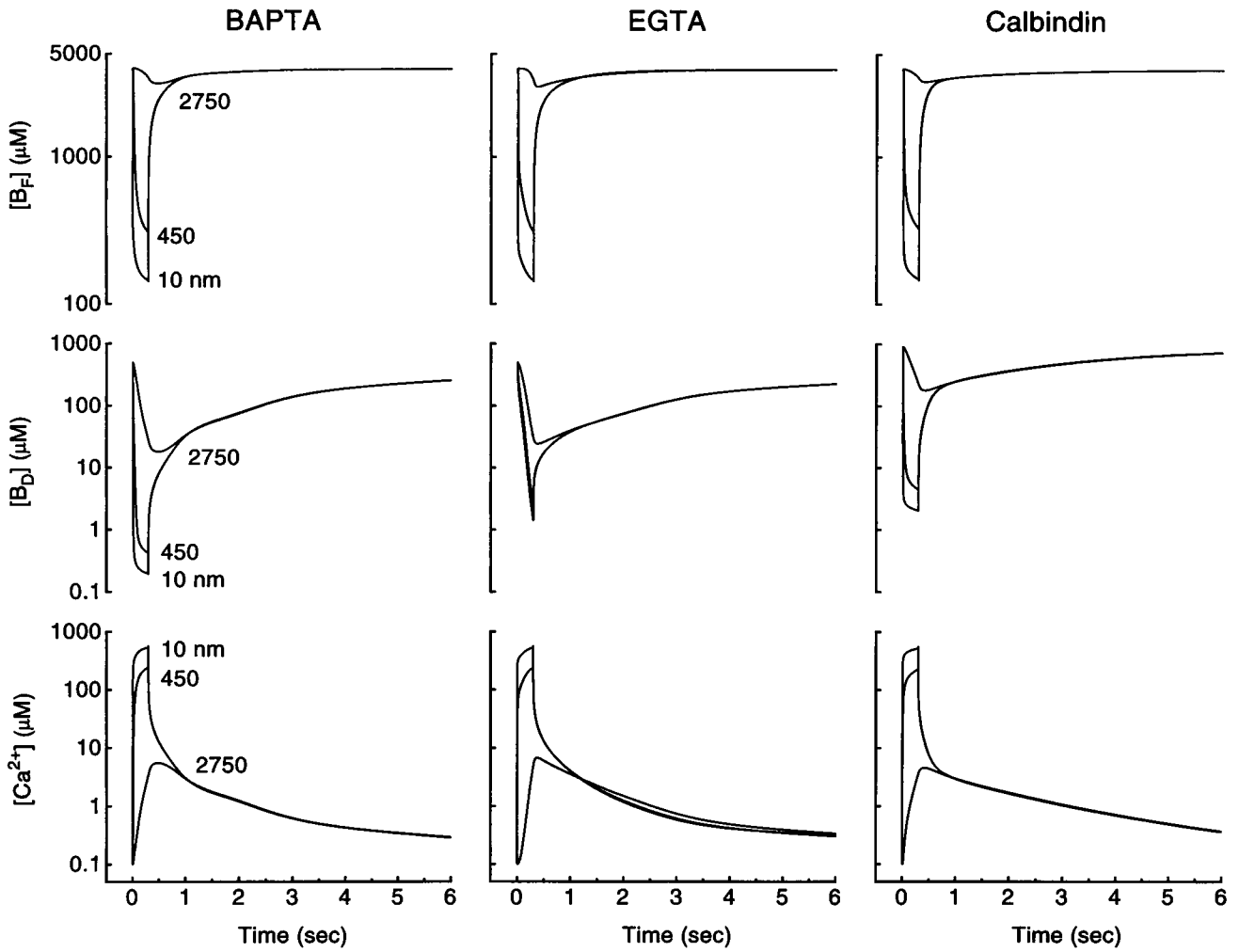

FIGURE 4 Effects of the identity of the diffusible buffer on changes in concentration of Ca^{2+}, fixed buffer, $[B_F]$, and diffusible buffer, $[B_D]$. Response to a voltage step from −80 to −20 mV computed at distances of 10, 450, and 2750 nm from the membrane along a radius from the center of the hotspot. The calculations were performed with 1 mM EGTA, 1 mM BAPTA, or 1 mM calbindin-28k as the diffusible buffer and a hotspot radius of 0.5 μm containing 157 Ca^{2+} channels (density, 200/μm^2).

less than 10 ms (5 mM BAPTA) compared with approximately 300 ms (1 mM BAPTA). Other properties of the mobile buffer were examined in the context of varying the buffer's identity, EGTA, BAPTA, and calbindin-28k. BAPTA has a faster rate constant for Ca^{2+} binding than the other two, and calbindin-28k has a 10-fold higher K_D (1 μM) than either BAPTA or EGTA and a 4-fold lower diffusion coefficient. These differences do not greatly affect the magnitude or speed of accumulation of Ca^{2+} beneath the hotspot (Fig. 4), but they affect the rate of consumption and restoration of free buffer. For example, the steady-state concentration of free calbindin-28k is restored faster after the pulse mainly because the buffer has a lower affinity than BAPTA or EGTA. Also, a greater fraction of calbindin-28k is uncomplexed in the resting state, which will enhance localization of Ca^{2+} at the hotspot.

An interesting example of the effects of buffer loading is the voltage dependence of Ca^{2+} accumulation, the results of which have implications for understanding Ca^{2+} modulation of intracellular processes. The Ca^{2+} current activates for membrane potentials positive to −55 mV, is maximal at approximately −20 mV, and then declines at more depolarized potentials due to a decreased driving force on Ca^{2+} entry. The Ca^{2+} concentration at the hotspot displayed a U-shaped relation similar to that of the current but was more steeply voltage dependent (Fig. 5). We interpret this effect as being caused by saturation of the buffers for the larger Ca^{2+} currents, which thus yields a higher Ca^{2+} concentration that increases nonlinearly with the Ca^{2+} current. If the Ca^{2+} at the hotspot were to trigger some secondary event, such as vesicle fusion, a study of the nonlinearity of the process may be misleading and lead to an overestimate of the Hill coefficient. This type of deviation will depend on a variety of parameters, including the magnitude of the Ca^{2+} flux (the channel density) and the concentrations and K_D of the Ca^{2+} buffers.

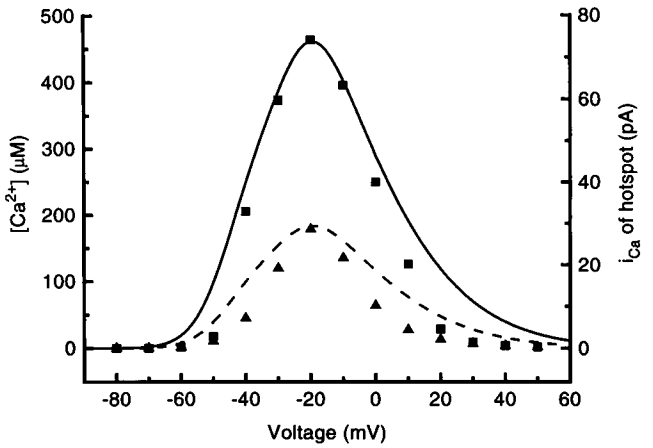

FIGURE 5 Voltage dependence of average Ca^{2+} concentration, $[Ca^{2+}]_{avghs}$, at hotspot measured at the end of a 10-ms (▲) or 300-ms (■) voltage step from −80 mV. Smooth curves give the voltage dependence of the Ca^{2+} current, the upper (continuous) curve being referred to the right-hand ordinate and the dashed curve being scaled from the continuous curve to match the maximal $[Ca^{2+}]$ for the 10-ms voltage step. The calculations were performed under standard conditions with 1 mM EGTA diffusible buffer and a hotspot radius of 0.5 μm containing 157 Ca^{2+} channels (density, 200/μm^2).

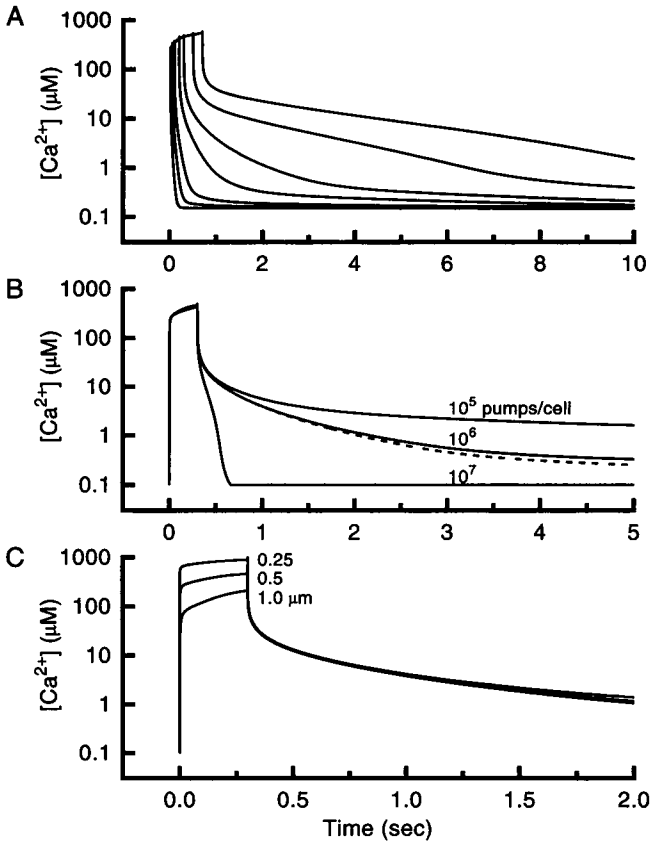

FIGURE 6 (*A*) Average Ca^{2+} concentration at hotspot, $[Ca^{2+}]_{avghs}$, for voltage steps from −80 to −20 mV of durations 10, 20, 50, 100, 300, 500, and 700 ms, 1 mM EGTA, and 10^6 CaATPase pumps/cell. (*B*) Average Ca^{2+} concentration at hotspot for 300-ms voltage steps from −80 to −20 mV with different numbers of CaATPase pumps of 10^5, 10^6, and 10^7/cell. For the three solid lines, the pumps were confined to the basal half of the cell; the dashed line is for a uniform pump distribution keeping the same density in the basal half of the cell, i.e., with a total of 2×10^6 pumps/cell. (*C*) Average Ca^{2+} concentration at hotspot for 300-ms voltage steps from −80 to −20 mV with hotspots of different radii (0.25, 0.5, and 1.0 μm) containing the same number of Ca^{2+} channels (157), 1 mM EGTA, and 10^6 pumps/cell.

Pulse duration and calcium pumps

The model allowed a study of some of the experimental manipulations used to draw conclusions about Ca^{2+} homeostatic mechanisms. These included the effects of pulse duration and the consequences of changing the number of Ca^{2+} pumps, achieved experimentally with blocking agents like vanadate and 2,4-di-(*t*-butyl) hydroquinone. Increasing the pulse duration from 10 to 700 ms (Fig. 6 *A*) was employed to vary the Ca^{2+} load over a wide range where the contribution of the various homeostatic mechanisms might differ. There were both fast and slow phases to the decay of Ca^{2+} around the hotspot, and lengthening of the pulse caused a progressive increase in the relative proportion of the slow components. However it was not easy to separate these into two uniquely defined constituents as was achieved in fitting the imaging data (Tucker and Fettiplace, 1995). The slow contribution arises mainly from the time required to unload the mobile buffer, this process being exacerbated at longer pulses by an increasing saturation of the fixed buffer. Consequently, as the Ca^{2+} falls, the fixed buffer continues to releases Ca^{2+} and maintain the mobile buffer in a complexed state. Thus, for pulse durations of more than 300 ms, the fixed buffer itself recovers with a slow time constant of several seconds. The complex kinetics evident in Fig. 6 *A* therefore reflect an interchange of Ca^{2+} between the fixed and the mobile buffers and the pump.

It is worth emphasizing that these complex kinetics are not conducive to easy characterization by fitting a small number of exponential time constants with a view to separating the underlying processes. It was therefore not possible to conclude that one time constant, perhaps stemming from Ca^{2+} diffusion away from the membrane, progressively increased with pulse duration whereas a slower component, perhaps due to Ca^{2+} removal from the cytoplasm, remained fixed. Nevertheless, changing the number of Ca^{2+} pumps from the standard number of 10^6/cell exclusively affected the slow phase of recovery (Fig. 6 *B*). A 10-fold increase in the number ensured that the Ca^{2+} returned to the baseline in less than 1 s whereas a 10-fold decrease in the number prolonged the recovery for more than 100 s. It is clear that the standard value provides the closest agreement with the experimental data. For most of the simulations, the pumps were restricted to the basal half of the cell to match the Ca^{2+} channel distribution. However, when the pumps were positioned over the entire cell, the recovery times were little affected, nor were the Ca^{2+} concentrations attained in at the hotspot or at the top of the cell.

Properties of the channel cluster and the spread of the Ca^{2+} signal

For a standard set of conditions, the properties of the cluster of Ca^{2+} channels were varied to examine their effects on the spread of intracellular Ca^{2+}. By comparing the simulations with the experimental measurements it was hoped to gain an insight into the structure of the hotspot. The standard condition was a hotspot of 0.5 μm radius with a channel density ρ^{h}_{Ca} of 200 μm^{-2}. This amounts to 157 channels in the cluster with an average spacing of approximately 70 nm. Two manipulations were performed: an increase in the hotspot size at a constant channel density and an increase in the hotspot size at a constant number of channels. Hotspot radii of 0.25, 0.5, and 1.0 μm were examined, which, at a constant channel density, correspond to 39, 157, and 623 channels, respectively (not shown). Higher densities or more channels both resulted in a higher local Ca^{2+} concentration. In both cases, the Ca^{2+} grew roughly in proportion to the change in area, which reflects Ca^{2+} flux across the membrane. The equivalent Ca^{2+} concentrations were approximately 200, 500, and 900 μM. An interesting aspect of the results was that for the three hotspots with the same channel numbers (Fig. 6 *C*) the recovery time courses were virtually identical. This presumably reflects the fact that the Ca^{2+} load was the same in the three cases.

One technique used to analyze the imaging data was to measure the rate of expansion of the hotspots as an indication of the diffusion of Ca^{2+} away from the membrane (Tucker and Fettiplace, 1995). A contour at a fixed gray level (corresponding to a threshold Ca^{2+} concentration) was drawn around the hotspot and the enclosed area determined in each frame during and after the depolarization. The plot of the enclosed area against time was approximately linear, with a slope the magnitude of which was comparable to the measured Ca^{2+} diffusion coefficient. The validity of this procedure was studied in the simulations by plotting the areal expansion at various Ca^{2+} thresholds from 1 to 50 μM. The results of the model, unlike those of the experiments, were nonlinear and also depended strongly on the value of the Ca^{2+} threshold chosen to construct the contours (Fig. 7 *A*). Nevertheless, if the results are viewed over a limited time scale of 500 ms at a Ca^{2+} threshold comparable to that used experimentally (14 μM), the average slope is approximately 25–50 $\mu m\ s^{-1}$. Linearization of the data may be a consequence of noise in the image combined with a much thicker section of at least 1 μm compared with 10 nm in the model. A useful feature of the experimental measurement was that it revealed changes in the growth of the hotspots due to changes in the Ca^{2+} buffering (Tucker and Fettiplace, 1995). This effect was reproduced by the model (Fig. 7 *B*), where for a fixed Ca^{2+} threshold, increasing the concentration of the mobile buffer drastically reduced the spot expansion. Both the slope and degree of nonlinearity were rather insensitive to the forward rate constant of the diffusible buffer (i.e., use of BAPTA or EGTA), but they were strongly dependent on the radius of the hotspot (Fig. 7 *C*).

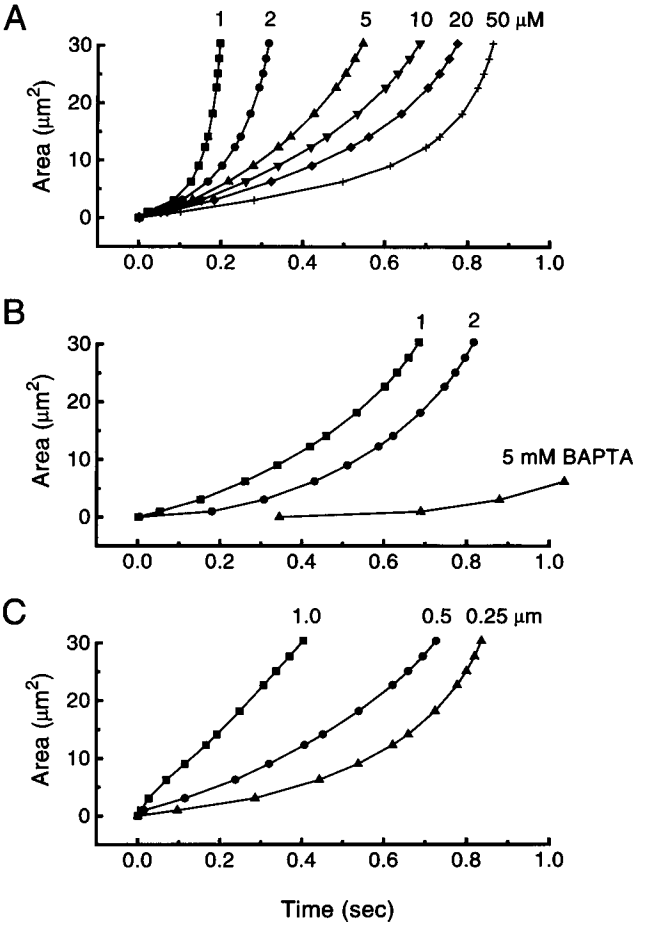

FIGURE 7 (*A*) Spread of Ca^{2+} signal from the center of the hotspot analyzed similarly to technique in Tucker and Fettiplace, 1995. A set of Ca^{2+} contours was drawn around the center of the hotspot corresponding to Ca^{2+} concentrations of 1, 2, 5, 10, 20, and 50 μM and the enclosed areas computed at different times after the onset of the voltage step from −80 to −20 mV with 1 mM BAPTA and a 0.5-μm radius hotspot. (*B*) Spread of the Ca^{2+} signal from the center of the hotspot for a threshold contour of 10 μM as a function of the concentration of diffusible buffer BAPTA (1, 2, and 5 mM) with a hotspot radius of 0.5 μm. (*C*) Spread of the Ca^{2+} signal from the center of the hotspot for a threshold contour of 10 μM as a function of the hotspot radius (0.25, 0.5, and 1.0 μm) with 1 mM BAPTA and a channel density of 200 μm^{-2}.

Ca^{2+} profiles across the hotspot

A method for displaying the degree of Ca^{2+} localization at the hotspot is to compute the Ca^{2+} concentration along a line passing through the hotspot's center. A series of longitudinal contours (running in the z direction) were taken 10 nm in from the membrane at various times during and after a 300-ms depolarizing step. Fig. 8 *A* shows that, under standard conditions with 1 mM BAPTA as the diffusible buffer, the Ca^{2+} is sharply confined to the hotspot for at least the first 10 ms of the depolarization. Both diffusible and fixed buffers exhibit equivalent behavior with the reduction in concentration of free buffer being confined to beneath the hotspot for the first 10 ms of the stimulus, although even on this time scale, significant depletion of the

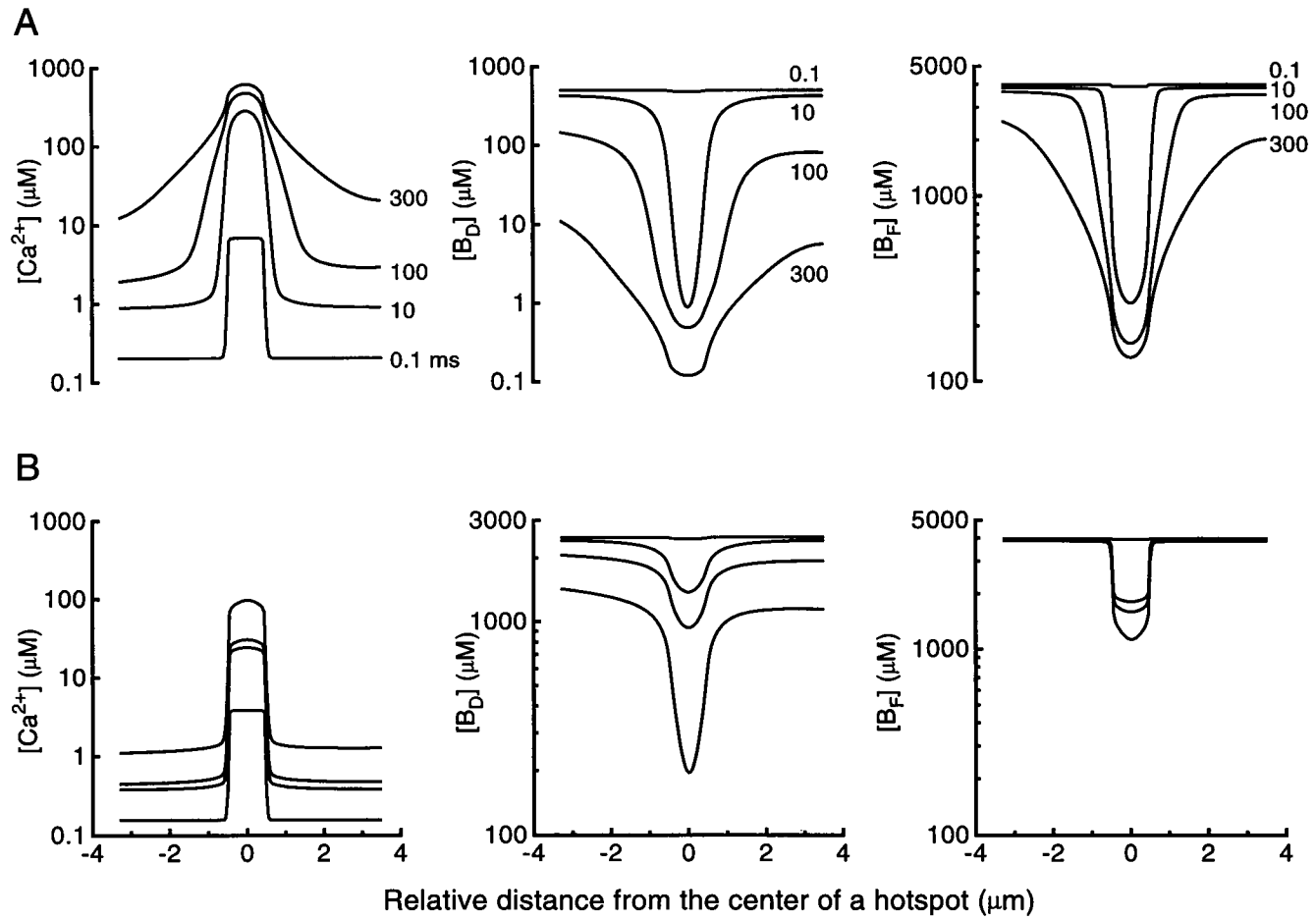

FIGURE 8 Longitudinal contours through a hotspot for changes in concentration of Ca^{2+} and fixed (B_F) and diffusible (B_D) buffers at different times after a voltage step to −20 mV. Traces of increasing concentration of Ca^{2+} and decreasing concentration of both buffers were taken at times 0.1, 10, 100, and 300 ms after the onset of the step. (*A*) Conditions were 4 mM fixed buffer, 1 mM diffusible buffer, BAPTA. (*B*) Conditions were 4 mM fixed buffer 5 mM diffusible buffer, BAPTA. Note that an increase in diffusible buffer improves Ca^{2+} localization. The center of the 0.5-μm radius hotspot is located at abscissa = 0 μm, the top of the cell to the left.

diffusible buffer occurs. For longer periods of 100 ms or more, changes in the concentration of Ca^{2+} and its buffers occur beyond the limits of the hotspot, the transition being marked by the point at which the diffusible buffer becomes depleted at the center of the hotspot (Fig. 8). Thus, the diffusible buffer at the hotspot is almost totally depleted by 10 ms and so additional Ca^{2+} entering at the hotspot can no longer be absorbed. Although free buffer is available in the surrounding region, it is unable to diffuse into the hotspot at a sufficient rate to match the rate of Ca^{2+} influx. As has been suggested from experimental measurements (Tucker and Fettiplace, 1995), the spread of the Ca^{2+} signal for more prolonged stimuli is a function of the Ca^{2+} buffers (Fig. 8). Increasing the concentration of BAPTA from 1 to 5 mM severely delimits the signals and at the same time reduces the maximal concentration changes. In contrast, reducing the amount of fixed buffer from 4 to 1 mM (not shown) causes concentration changes over a much wider area .

The results in Fig. 8 indicate that, at a critical point defined by the combination of stimulus duration and concentration of Ca^{2+} buffers, the degree of localization deteriorates. Another means of revealing this change is to examine the interaction between two neighboring hotspots, effectively determining the resolution of the Ca^{2+} signal (Fig. 9). Two channel clusters, each 0.5 μm in diameter, were placed side by side in the z direction with centers 1 μm apart. In a standard intracellular medium containing 1 mM BAPTA, the Ca^{2+} microdomains remained distinct for at least 10 ms; fusion of the hotspots, apparent in the 200-ms trace, was associated with serious depletion of the diffusible buffer in the vicinity of the hotspot. The degree of overlap of the two hotspots depended on the concentration of diffusible Ca^{2+} buffer and on the parameters of the channel cluster; greater Ca^{2+} fluxes or reduced buffer concentration were both marked by a larger overlap at earlier times. The use of calbindin rather than BAPTA as the diffusible buffer had no major effect on the Ca^{2+} profile across the hotspots. However, decreasing the diffusion coefficient of calbindin from 100 to 25 $\mu m^2\ s^{-1}$ was found to increase the overlap, thus decreasing the resolution of the Ca^{2+} signals. This effect is caused mainly by a slower replenishment of free

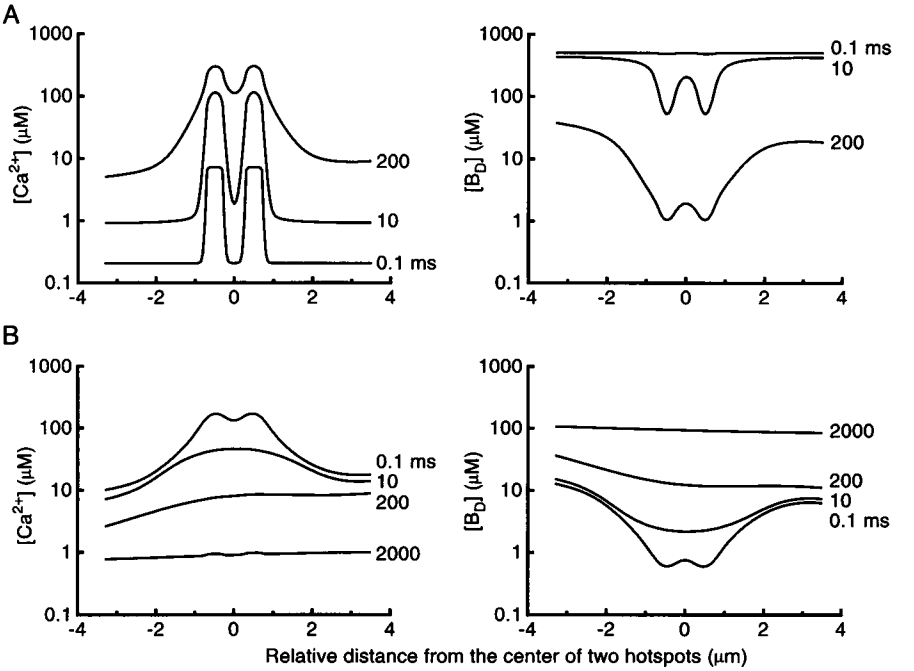

FIGURE 9 Longitudinal contours through two neighboring hotspots for changes in concentration of Ca^{2+} and diffusible (B_D) buffer at different times during and after a 300-ms voltage step to −20 mV. (*A*) Traces of increasing concentration of Ca^{2+} and decreasing concentration of buffer were taken at times 0.1, 10, and 200 ms after the onset of the depolarizing step. (*B*) Traces of decreasing concentration of Ca^{2+} and increasing concentration of buffer were taken at times 0.1, 10, 200, and 2000 ms after the end of the step. The centers of the 0.25-μm radius hotspots are located 1 μm apart, the top of the cell to the left. Same conditions as Fig 8 *A*.

buffer at the hotspot by its diffusion from the surrounding region; the more immobile the buffer, the less it contains the Ca^{2+} signals. This observation emphasizes the importance of the diffusible buffer for Ca^{2+} localization (Roberts, 1994).

The results in Figs. 8 and 9 provide an indication of the extent to which two neighboring hotspots can function independently. The afferent release sites of turtle hair cells are separated on average by a few microns from each other as well as from the efferent terminals (see Fig. 6 of Sneary, 1988). This spacing would enable the Ca^{2+} signals to remain independent at least for frequencies of 100 Hz or more. Independence could be maintained at lower frequencies by reducing the Ca^{2+} current, which is a known property of turtle hair cells tuned to low frequencies (Art et al., 1993).

The speed of the hotspot's Ca^{2+} signal

In normal operation of turtle hair cells the changes in Ca^{2+} with depolarization must be fast enough to enable the cells to process acoustic stimuli up to frequencies of ~1 kHz. The kinetics of the Ca^{2+} signals were defined with short 10-ms depolarizing pulses, and the effects of varying the properties of the channel cluster and the Ca^{2+} buffering were examined. The Ca^{2+} signals for a step depolarization to −20 mV possessed fast and slow kinetics components (Fig. 10 *A*), with an initial rapid phase and a slower creep visible both at the onset and offset of the pulse. Maximizing the speed with which the Ca^{2+} changes largely involves minimizing the contribution of the slow component. The relative contribution of the slow phase depended partly on the size of the channel cluster (Fig. 10 *A*), so that for a fixed channel density, the smaller the cluster, the faster the excursion. A second effect was that the Ca^{2+} level achieved during the step depended on the number and density of channels. Higher densities or more channels both resulted in a higher local Ca^{2+} concentration that, as discussed above (see Fig. 6), are configurations that maximize the Ca^{2+} flux across the membrane. Therefore, the largest and fastest excursion in Ca^{2+} at the hotspot was produced by a small dense cluster of Ca^{2+} channels.

The other major factor to influence the Ca^{2+} dynamics is the concentration of the diffusible buffer, and Fig. 10, *B–D* shows the effects of varying the concentration of BAPTA from 0.1 to 5 mM. For these simulations, in contrast to the others, the depolarizing stimulus was confined to a voltage step from −50 to −45 mV, which encompasses the range used to define the kinetics of the Ca^{2+}-activated K^+ currents and the electrical resonant frequency of turtle hair cells (Art and Fettiplace, 1987; Wu et al., 1995). The consequences of employing channel clusters of different dimensions in limiting the kinetics of the Ca^{2+} changes are accentuated by the linear plots. These linear plots reinforce the conclusion that the most rapid excursions are achieved with the smallest spot sizes, and for spot diameters of 0.125 and 0.25 μm radius a limiting behavior is achieved with a virtual absence of a secondary slow component. In contrast, with the two larger hotspot sizes, a secondary component is present that becomes more pronounced at the lower buffer concentrations. The primary role of the diffusible buffer is best illustrated by the traces for the 0.5-μm radius hotspot. Comparison of Fig. 10, *B*, *C*, and *D* shows that increasing the BAPTA concentrations reduced the Ca^{2+} level over 10-fold during the pulse from 85 to 6.5 μM and accelerated the onset times.

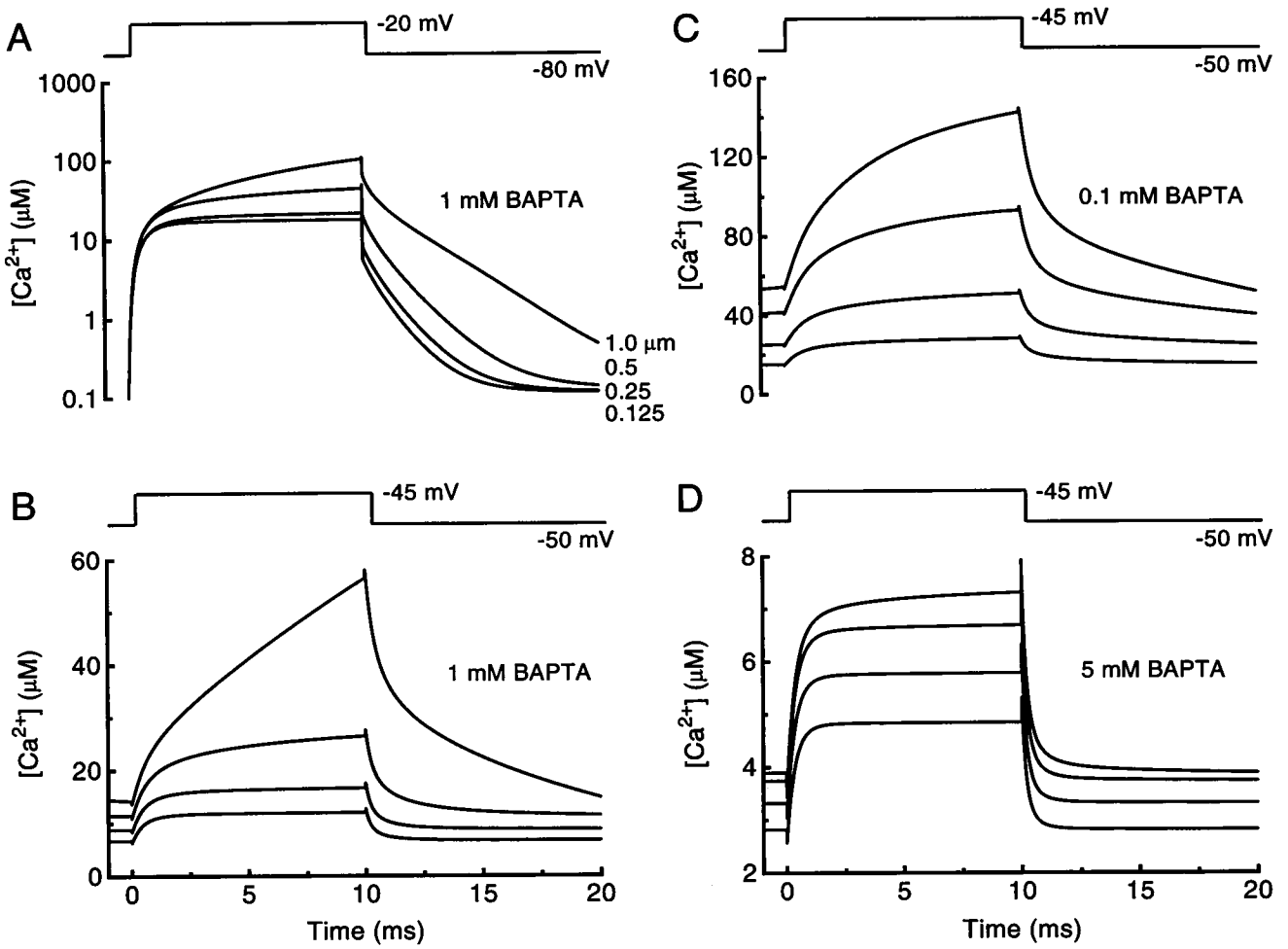

FIGURE 10 Effects of hotspot parameters and diffusible buffer on average Ca^{2+} changes, $[Ca^{2+}]_{avghs}$, to brief depolarizations. (*A*) Fixed density of Ca^{2+} channels inside hotspot, 200 μm^{-2}; hotspot radii, 1.0, 0.5, 0.25, and 0.125 μm; 1 mM BAPTA. (*B*) Diffusible buffer, 1 mM BAPTA; Ca^{2+} channel density, 200 μm^{-2}; hotspot radii (from top trace to bottom trace), 1.0, 0.5, 0.25, and 0.125 μm. (*C*) Diffusible buffer, 0.1 mM BAPTA; Ca^{2+} channel density, 200 μm^{-2}; hotspot radii (from top trace to bottom trace), 1.0, 0.5, 0.25, and 0.125 μm. (*D*) Diffusible buffer, 5 mM BAPTA; Ca^{2+} channel density, 200 μm^{-2}; hotspot radii (from top trace to bottom trace), 1.0, 0.5, 0.25, and 0.125 μm. Note that the Ca^{2+} concentration scale is logarithmic in *A* and linear in *B*, *C*, and *D*. The voltage step, shown above, was from −80 to −20 mV in *A* and −50 to −45 mV in *B*, *C*, and *D*.

Owing to the complex kinetic effects of diffusion and buffering, the time course of Ca^{2+} concentration changes have been represented in hair cell simulations by a simple first-order differential equation (Hudspeth and Lewis, 1988; Wu et al., 1995; Wu and Fettiplace, 1996). This equation relates the Ca^{2+} current flowing through Ca^{2+} channels and the Ca^{2+} concentration near the membrane $[Ca_m^{2+}]$:

$$\frac{d[Ca_m^{2+}]}{dt} = S_F \cdot i_{Ca} \cdot p_{Ca} - k_R \cdot [Ca_m^{2+}], \qquad (23)$$

where S_F and k_R are constants embodying the gain and speed of the local Ca^{2+} handling processes. It is clear that Eq. 23 is a crude approximation, and even for small or brief excursions in membrane potential, the changes in Ca^{2+} are nonlinear. Nevertheless, a rough estimate of the time constant $(k_R)^{-1}$ can be derived from the onsets of the responses in Fig. 10, *B–D*, which could be reasonably fitted with a single exponential (the offsets required at least two exponentials). The time constant grew with both increase in hotspot size and reduction in buffer concentration. These trends may be illustrated by the following examples: 1) for the standard 0.5-μm radius hotspot, the time constants were 1.8, 1.2, and 0.4 ms for 0.1, 1, and 5 mM BAPTA, the value at the highest buffer concentration asymptoting to the onset time constant of the current (approximately 0.3 ms); 2) for 1 mM BAPTA, the time constants were 0.5, 0.6, 1.2, and 5.5 ms for increasing radii from 0.125 to 1 μm. Thus, for the smallest channel clusters in the presence of millimolar diffusible buffer, the time constant $(k_R)^{-1}$ is no more than a few tenths of a millisecond.

Sinusoidal responses and phase locking

In view of the complex time course of the changes in Ca^{2+} during step depolarizations, the temporal filtering introduced by the hotspot was also quantified using sinusoidal

excursions in membrane potential (Fig. 11). This approach provided an alternative measure of the frequency response for stimuli that may approximate those normally encoded by the hair cells due to their sharply resonant behavior. The hair cell's membrane potential was set to −50 mV and subjected to modulations 5 mV in amplitude at frequencies from 50 to 1000 Hz, thus encompassing the turtle's normal acoustic range. (It is worth noting that hair cells in the intact turtle's cochlea have resting potentials of approximately −50 mV, superimposed on which is a narrow band noise up to 5 mV in amplitude; see Fig. 18 of Crawford and Fettiplace, 1980.) For these stimuli, the Ca^{2+} current and average Ca^{2+} beneath the hotspot, $[Ca^{2+}]_{avghs}$, followed sinusoidally, but both declined with frequency. The frequency dependence is plotted in Fig. 12, with the responses normalized to their values at 50 Hz. The measurements (solid diamonds) derived from the traces in Fig. 11, *A* and *B*, have a corner frequency (at which the normalized response drops to $1/\sqrt{2}$) of 200 Hz and fall off at high frequency with a slope of approximately 1. As expected from the results in Fig. 10, both the number of channels and the amount of diffusible buffer influence the corner frequency. Thus, with larger diameter hotspots containing more channels, the corner frequency was lowered. In contrast, elevating the concentration of BAPTA to 5 mM increased the corner frequency to approximately 500 Hz. However, the wider band-width was coupled to a reduction in the maximal amplitude of the Ca^{2+} concentration changes. With identical hotspot dimensions, the Ca^{2+} excursion was 8.2 μM with 1 mM BAPTA and 2.5 μM with 5 mM BAPTA. This correlation may have important implications for optimizing the speed of synaptic transmission in the auditory pathway (see Discussion).

The synapse between the hair cell and the VIIIth nerve afferent is unusual in that it operates on graded changes in the membrane potential of the presynaptic cell, which mod-

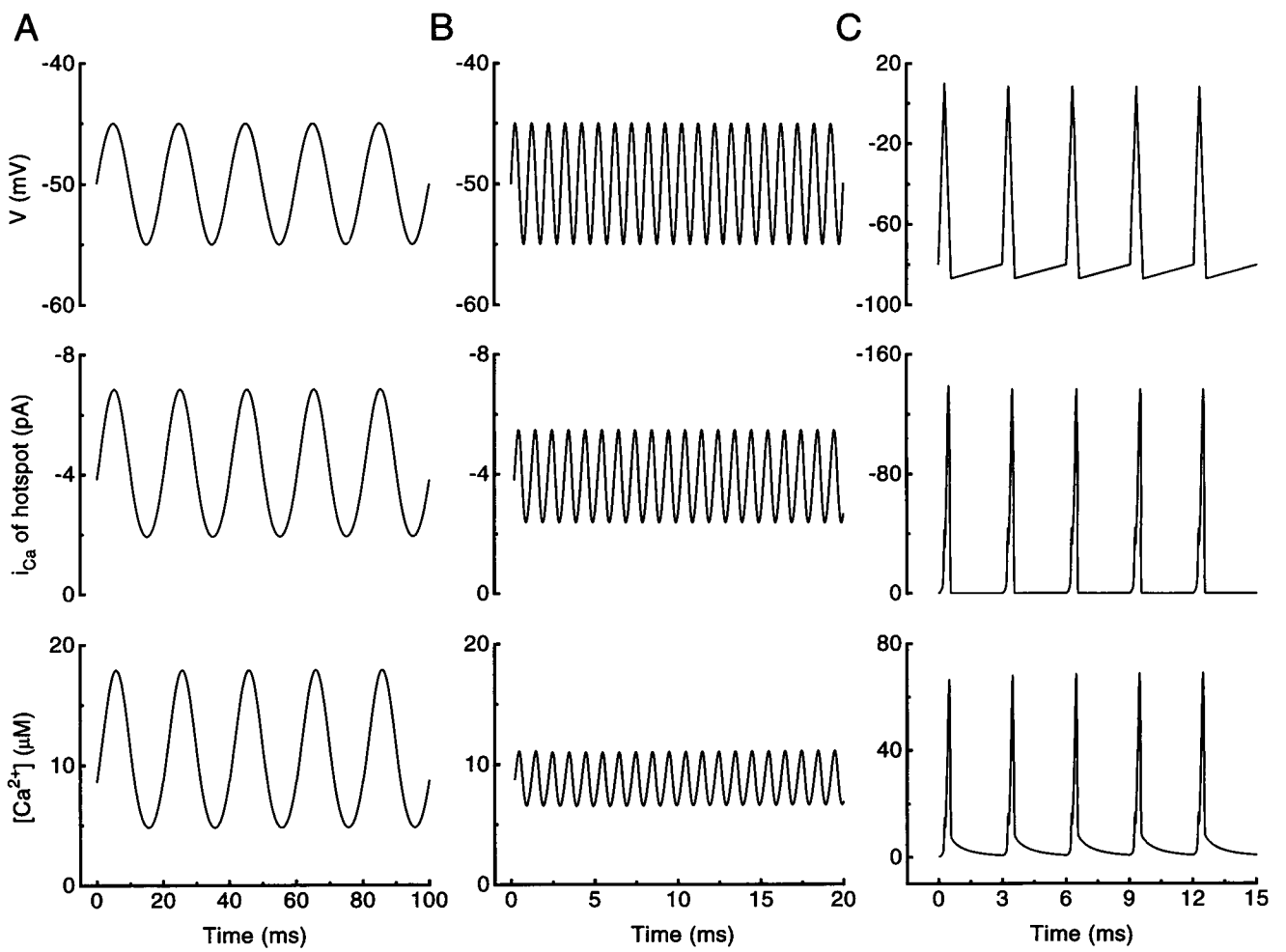

FIGURE 11 Changes in Ca^{2+} current (middle traces) and average Ca^{2+} concentration, $[Ca^{2+}]_{avghs}$, at the hotspot (bottom traces) in response to periodic modulation of the membrane potential (top). (*A*) Response for a 50-Hz sinusoid of amplitude 5 mV modulated about −50 mV. (*B*) Response for a 1000-Hz sinusoid of amplitude 5 mV modulated about −50 mV. (*C*) Response for a 300-Hz train of 90-mV action potentials of 0.5-ms half-width from −80 mV. It should be noted that hair cells do not normally generate action potentials; the amplitude and duration of the voltage wave form were based on action potentials seen in lower vertebrate auditory nerve fibers. All responses are for a 0.25-μm radius hotspot with 200 channels/μm^2 and 1 mM BAPTA as diffusible buffer.

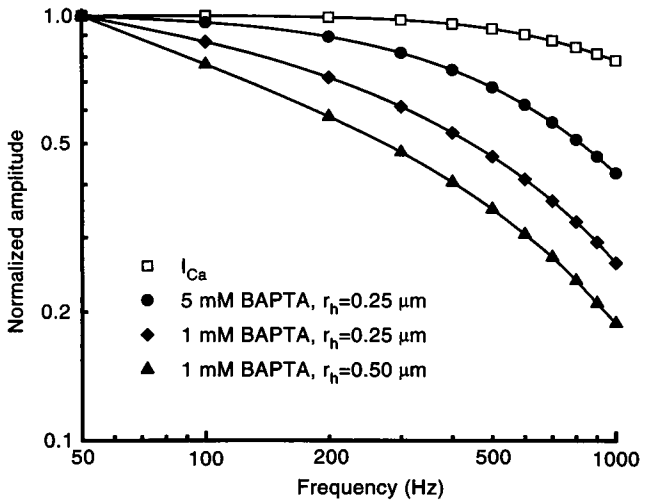

FIGURE 12 Frequency dependence of amplitude of the Ca^{2+} current (□) and average Ca^{2+} concentration, $[Ca^{2+}]_{avghs}$, at the hotspot (●, ◆, and ▲). The membrane potential was modulated sinusoidally about −50 mV with an amplitude of 5 mV as in Fig. 11, *A* and *B*. ▲, 0.5-μm radius hotspot, 200 channels/μm², 1 mM BAPTA diffusible buffer; ◆, 0.25-μm radius hotspot, 200 channels/μm², 1 mM BAPTA diffusible buffer; ●, 0.25-μm radius hotspot, 200 channels/μm², 5 mM BAPTA diffusible buffer. In a given condition, the response amplitudes have been normalized to the value at 50 Hz. Resting Ca^{2+} concentrations and maximal amplitudes are as follows: ▲, 11.6 μM, 14.7 μM; ◆, 8.8 μM, 8.2 μM; ●, 3.3 μM, 2.5 μM. Note that the best frequency response is obtained with the highest BAPTA concentration but is associated with the smallest modulation amplitude.

ulate the release of chemical transmitter about a steady level. Although tonic release of transmitter may depend on a specialized mechanism of exocytosis associated with synaptic ribbons or dense bodies, the mechanisms underlying influx and buffering of Ca^{2+} are probably similar in all neurons. For example, in the auditory brainstem, the presynaptic Ca^{2+} current, although mainly of the N type blockable by ω-conotoxin GVIA, activates between −50 and −10 mV with fast kinetics and so functionally resembles Ca^{2+} currents in hair cells (Sivaramakrishnan and Laurent, 1995). We therefore examined the performance of the hotspots during stimulation with an action potential, although it must be emphasized that hair cells do not normally produce such action potentials. The waveform of the action potential consisted of a 90-mV triangular depolarization of 0.5 ms half-width from a resting potential −80 mV, followed by a 10-mV undershoot (Fig. 11 *C*). There was an initial component of Ca^{2+} current during the rising phase of the action potential and a larger secondary component, equivalent to a tail current, during the repolarizing phase of the action potential. The delineation of the two components of Ca^{2+} current most likely stems from the fast kinetics and low-threshold activation of the auditory Ca^{2+} channels. The resulting elevation in Ca^{2+} concentration beneath the hotspot comprised a fast transient component mirroring the current, followed by a slower return to baseline. The amplitude of the Ca^{2+} concentration change depended on the geometry of the hotspots and the buffer, and under standard conditions the fast transient attained a concentration of approximately 70 μM. The Ca^{2+} transient was sufficiently rapid to sustain a firing rate of 300 Hz without significant elevation in the resting Ca^{2+} concentration.

DISCUSSION

General conclusions

The aim of the present analysis was to construct a model with fine enough resolution to describe the changes in Ca^{2+} beneath the membrane near a cluster of channels, while at the same time accounting for the Ca^{2+} balance across the entire cell, thus embracing a wider temporal and spatial extent than in previous simulations. The model has been calibrated against Ca^{2+} measurements obtained in hair cells and has then been extended to predict the Ca^{2+} behavior under conditions that were experimentally inaccessible. The model reproduces many features of the Ca^{2+} microdomains observed with confocal imaging (Tucker and Fettiplace, 1995) and shows good agreement with the range of concentration changes (Figs. 2 and 3), the rate of expansion of the Ca^{2+} microdomains (Fig. 7), and the effects of buffers on localization (Figs. 7 *B* and 8). The model is also consistent with the experimental effects of varying pulse duration and number of CaATPase pumps (Fig. 6, *A* and *B*), although there are quantitative discrepancies. In particular, the experimentally observed decline in Ca^{2+} concentration after a load was dominated by a component with a time constant (around 100 ms) the value of which varied with pulse duration and Ca^{2+} removal rate. In contrast, the model predicted that the major kinetic components were much faster and that a higher Ca^{2+} concentration was achieved at the center of the hotspot. These differences may be partly due to the spatial and temporal averaging required in the imaging experiments (see Fig. 3 *C*). Small errors in positioning the confocal plane and the measurement area relative to the hotspot membrane could lead to substantial errors in the size and speed of the Ca^{2+} transients; they may also account for the apparent inability to define single release sites experimentally. Local saturation of Calcium Green 5N, the calcium dye ($K_D \approx 30$ μM) used in the experiments, would also contribute to spatial and temporal distortion of the Ca^{2+} changes. Similar experimental problems may accrue from use of the SK channel as a Ca^{2+} indicator (Tucker and Fettiplace, 1996), as those channels are likely to be distributed over a range of distances form the hotspot and, with a $K_D \approx 2$ μM, will be saturated by Ca^{2+} concentrations attained at the center.

The model also makes predictions in two general areas. First, it indicates how the magnitude and time course of the Ca^{2+} response might depend on the hotspot geometry (Figs. 6 *C*, 7 *C*, and 10) and on the concentration of diffusible buffer (Figs. 8, 10, and 12). Smaller hotspots (under constant channel density) and higher buffer concentrations result in faster but smaller Ca^{2+} transients. The physiological

significance of this prediction is discussed below. Second, it raises a number of instances where the kinetics and localization of the Ca^{2+} signals are influenced by depletion of buffer (e.g., Figs. 5, 7, 8, and 10). Our conclusions are broadly in line with those of Roberts (1994), whose modeling emphasized the contribution of a mobile Ca^{2+} buffer like calbindin-D28k, which by shuttling Ca^{2+} away from the channel clusters limits the magnitude and distribution of the Ca^{2+} changes.

A major source of uncertainty in the model pertains to the fixed buffer, the concentration and K_D of which were chosen to generate a buffering capacity of ~200 as measured experimentally (Tucker and Fettiplace, 1995). The K_D of 20 μM is arbitrary and results in the depletion of the fixed buffer when the Ca^{2+} exceeds the buffer's K_D. This is clearly unrealistic, and it is likely that the fixed buffer in the intact hair cell includes multiple components, both cytoplasmic constituents and organelles, with a range of K_D values to prevent catastrophic elevation in the free Ca^{2+}. More experimental information about the Ca^{2+} buffering of the cytoplasm, especially that contributed by organelles like mitochondria (Gunter and Pfeiffer, 1990) and smooth endoplasmic reticulum, would help refine the model and determine whether buffer depletion plays a significant role in shaping the Ca^{2+} transients.

Hotspot geometry

It is functionally important to the hair cell that the Ca^{2+} signals at the hotspot follow rapidly on the gating of the Ca^{2+} channels. This ensures that changes in Ca^{2+} concentration are not rate limiting either in releasing chemical transmitters onto the afferent terminals to produce phase locking up to 1 kHz or in gating of the K_{Ca} channels, which underlies electrical resonance up to frequencies of 600 Hz (Crawford and Fettiplace, 1980; 1981). Furthermore, the Ca^{2+} signals must be of sufficient magnitude to activate the K_{Ca} channels and trigger the transmitter release mechanism. The results in Fig. 10 indicate that average Ca^{2+} concentrations of 10–100 μM can develop and dissipate rapidly. Such concentrations would be adequate to drive the synaptic release process characterized in retinal bipolar cells by Heidelberger et al. (1994). Hotspots of 0.5–1 μm diameter will contain 40–160 channels at a density of 200/μm^2 used in the calculations. A mid-frequency turtle hair cell tuned to 250 Hz will have approximately 1600 Ca^{2+} channels (Wu et al., 1995) and 15–20 release sites (Sneary, 1988). Each site therefore contains approximately 100 channels assuming all sites observed histologically are functional. These numbers are very similar to those of Roberts et al. (1990) who calculated an average of 1900 Ca^{2+} channels in 19 release sites in frog hair cells yielding approximately 95 channels/site. In the turtle cochlea, both the number of Ca^{2+} channels (Wu et al., 1995) and the number of release sites per cell (Sneary, 1988) increase with resonant frequency, F_o, (i.e., with location in the cochlea). These observations suggest a similar number of channels per site.

An increase in the amount of buffer, although reducing the Ca^{2+} concentration, accelerates the kinetics so that, with 5 mM BAPTA, the average Ca^{2+} produces rapid transients (Fig. 10 *D*) and will follow a sinusoidal voltage up to 600 Hz with little attenuation (Fig. 12). For comparison, the speed of synaptic transmission in hair cells can be estimated from the degree of synchronization of the afferent firing. In lower vertebrates at room temperature afferent synchronization has a corner frequency of 340–500 Hz in frog, alligator lizard (Weiss and Rose, 1988), and turtle (Crawford and Fettiplace, unpublished observations). Whether the kinetics of Ca^{2+} signals are a limiting factor in synaptic transmission is unclear, but an important factor may be the use of multiple release sites, each site being small enough to ensure that the average Ca^{2+} changes are rapid. One hypothesis to account for the design of the release sites is that the number of Ca^{2+} channels, release sites, and cytoplasmic Ca^{2+} buffer are co-regulated to optimize the speed of synaptic transmission. Thus, hair cells at the base of the cochlea must process higher frequency signals; they may have more Ca^{2+} buffer to handle the larger Ca^{2+} load resulting from a greater number of channels. The larger amount of cytoplasmic Ca^{2+} buffer speeds up the Ca^{2+} transients at each release site, but it also lowers the peak Ca^{2+} concentration at each site. Hence, to achieve the same total output of chemical transmitter requires a larger number of release sites in hair cells tuned to higher frequencies. We propose that there is an increase in the Ca^{2+} buffer concentration in high-frequency hair cells that allows lower amplitudes and faster Ca^{2+} responses at a larger number of release sites.

The above arguments are based entirely on the average Ca^{2+} concentration beneath the hotspot and require only that the trigger molecules, the K_{Ca} channels or vesicle release apparatus, be located among the array of Ca^{2+} channels (Roberts et al., 1990). A more detailed scheme would include an array of discrete channels introducing spatial heterogeneity in the hotspot. With the alternative discrete model, the Ca^{2+} changes close to the channels would be larger and would follow more faithfully the time course of the current. Therefore, placing the trigger proteins adjacent to (within 10 nm of) the Ca^{2+} channels will produce the fastest responses limited only by local Ca^{2+} diffusion. This approach was employed in reconstruction of the electrical resonance (Wu et al., 1995). Assuming the Ca^{2+} channels are placed on a square grid at a density of 200/μm^2 the mean channel spacing is approximately 70 nm, so no point is more than 50 nm from a Ca^{2+} channel. Analysis of this more complex model requires a different approach that was not attempted here. However, an estimate of the discrepancy can be obtained by comparing the 10-nm and 80-nm traces in Fig. 3 *B*. After 10 ms, the response at 10 nm from the membrane is 280 μM, approximately 15% larger than the response at 80 nm. More significantly, the 10-nm response leads the 80-nm response by approximately 0.5 ms at half-amplitude suggesting that an increased frequency response may be obtained for the Ca^{2+} changes in a discrete channel model.

This work was supported by a research grant (5 R01 DC01362) to R. Fettiplace from the National Institute on Deafness and Other Communication Disorders, National Institutes of Health.

APPENDIX

Numerical methods and difference equations

To select an appropriate numerical method is critical in increasing the accuracy and reducing the computational load. The complexity of the system, however, excludes several approaches. The existence of hotspots necessitates using a three-dimensional model, and high spatial resolution is also required due to the relatively small dimensions of a hotspot of radius 0.125–1 μm. Thus, the simple forward-Euler algorithm becomes undesirable because the criterion of stability for this specific method (Strikwerda, 1989; Mascagni, 1989) demands enormous computational work, which increases the difficulty for simulations longer than 1 s with present computational facilities (Yamada and Zucker, 1992). To overcome the obstacle, a combined approach of variable grid sizes and an implicit alternative-direction modification of the Crank-Nicolson method for three dimensions (Douglas and Rachford, 1956; Douglas, 1962) was applied to maintain the stability in convergence as well as reduce the computation time. The analytic solution was used to solve the ordinary differential equation for the kinetics of the Ca^{2+} current. The predictor-corrector explicit scheme was used to integrate the ODE describing the fixed buffer (Yamada et al., 1989).

The difference equations of first- and second-order derivatives for a variable-grid approach are slightly different from a fixed-grid approach. By rearranging the backward and forward difference equations from Taylor's expansion (Smith, 1965, pp. 139–140), the first-order derivative in the r direction can be approximated as

$$\nabla_r u_i \approx \frac{u_{i+1} - u_{i-1}}{\Delta_i + \Delta_{i+1}} = c_i(u_{i+1} - u_{i-1}), \tag{A1}$$

where c_i is equal to $1/(\Delta_i + \Delta_{i+1})$. Similarly, the second-order derivative can be approximated by canceling out the first-order derivative and ignoring the high-order (Smith, 1965, pp. 139–140):

$$\nabla_r^2 u_i \approx \frac{2[\Delta_{i+1}(u_{i-1} - u_i) + \Delta_i(u_{i+1} - u_i)]}{\Delta_i\Delta_{i+1}(\Delta_i + \Delta_{i+1})}$$

$$= a_i u_{i-1} - (a_i + b_i)u_i + b_i u_{i+1}, \tag{A2}$$

where a_i and b_i are equal to $2/[\Delta_i(\Delta_i + \Delta_{i+1})]$ and $2/[\Delta_{i+1}(\Delta_i + \Delta_{i+1})]$, respectively. The same approach can be applied to the θ and z direction using the indices j and k, respectively:

$$\nabla_\theta u_j \approx \frac{u_{j+1} - u_{j-1}}{\Delta_j + \Delta_{j+1}} = c_j(u_{j+1} - u_{j-1}), \tag{A3}$$

$$\nabla_z u_k \approx \frac{u_{k+1} - u_{k-1}}{\Delta_k + \Delta_{k+1}} = c_k(u_{k+1} - u_{k-1}), \tag{A4}$$

$$\nabla_\theta^2 u_j \approx a_j u_{j-1} - (a_j + b_j)u_j + b_j u_{j+1}, \tag{A5}$$

$$\nabla_z^2 u_k \approx a_k u_{k-1} - (a_k + b_k)u_k + b_k u_{k+1}, \tag{A6}$$

where a_j, b_j, c_j, a_k, b_k, and c_k are equal to $2/[\Delta_j(\Delta_j + \Delta_{j+1})]$, $2/[\Delta_{j+1}(\Delta_j + \Delta_{j+1})]$, $1/(\Delta_j + \Delta_{j+1})$, $2/[\Delta_k(\Delta_k + \Delta_{k+1})]$, $2/[\Delta_{k+1}(\Delta_k + \Delta_{k+1})]$, and $1/(\Delta_k + \Delta_{k+1})$, respectively. In the simulation, the size of the compartment in the r direction gradually expanded from 0.02 to 0.1 μm at 0.2 μm from the center of hotspot and to 0.2 μm at 0.5 μm from the center of hotspot; in the θ direction from 0.4° to 1° at 6.8° from the hotspot and to 12° at 23.8° from the hotspot; and in the z direction from 0.025 to 0.1 μm at 0.275 μm from the hotspot and to 0.5 μm at 3.475 μm from the hotspot. The closer to the hotspot, the smaller was the compartment used. The validity of the model was tested by comparison with two models, one a two-dimensional model with fixed 0.1-μm grid size in both r and z directions under uniform distribution of Ca^{2+} channels and the other a finer three-dimensional model with grid sizes reduced to 0.01 μm, 0.1°, and 0.01 μm in the r, θ, and z directions, respectively. The time interval for integration was varied according to the time lag after a step change of membrane potential; e.g., for a standard 300-ms step, the time interval gradually increased from 0.001 to 0.01 ms after 5 ms, to 0.1 ms after 20 ms, to 1 ms after 200 ms, and to 10 ms after 10 s. Finer intervals were used for simulations of the sinusoidal excursion and the action potentials.

The implicit alternative-direction method is generalized in the following equations with two intermediate values that represent the successive approximations toward u^{n+1}:

$$\frac{u^* - u^n}{\Delta t} = D_u\left[\frac{1}{2}\nabla_r^2(u^* + u^n) + \frac{1}{2r_i}\nabla_r(u^* + u^n) + \frac{1}{r_i^2}\nabla_\theta^2 u^n + \nabla_z^2 u^n\right] + \frac{\Psi(u^*) + \Psi(u^n)}{2}, \tag{A7}$$

$$\frac{u^{**} - u^n}{\Delta t} = D_u\left[\frac{1}{2}\nabla_r^2(u^* + u^n) + \frac{1}{2r_i}\nabla_r(u^* + u^n) + \frac{1}{2r_i^2}\nabla_\theta^2(u^{**} + u^n) + \nabla_z^2 u^n\right] + \frac{\Psi(u^{**}) + \Psi(u^n)}{2}, \tag{A8}$$

$$\frac{u^{n+1} - u^n}{\Delta t} = \frac{D_u}{2}\left[\nabla_r^2(u^* + u^n) + \frac{1}{r_i}\nabla_r(u^* + u^n) + \frac{1}{r_i^2}\nabla_\theta^2(u^{**} + u^n) + \nabla_z^2(u^{n+1} + u^n)\right] + \frac{\Psi(u^{n+1}) + \Psi(u^n)}{2}, \tag{A9}$$

where D_u is the diffusion coefficient of substance u and $\psi(\bullet)$ is a function where the first successive approximation at (r_i,θ_j,z_k) is for example defined as follows:

$$\Psi([B_D]^*) = k_D^d k_D^+([B_D^T] - [B_D]^*) - k_D^+[Ca^{2+}]^n[B_D]^*, \tag{A10}$$

$$\Psi([Ca^{2+}]^*) = \frac{2\nu_{max}A_{ijk}}{\Delta_i\Delta_j\Delta_k(2r_i - \Delta_i)} \cdot\left\{\frac{[Ca^{2+}]_o}{[Ca^{2+}]_o + K_m} - \frac{[Ca^{2+}]^*}{[Ca^{2+}]^n + K_m}\right\} - \frac{n_{Ca}(i,j,k)\bar{i}_{Ca}(t)}{\Delta_i\Delta_j\Delta_k(2r_i - \Delta_i)F} + k_F^d k_F^+ \cdot([B_F^T] - [B_F]^{n+1}) - k_F^+[Ca^{2+}]^*[B_F]^{n+1} + k_D^d k_D^+([B_D^T] - [B_D]^{n+1}) - k_D^+[Ca^{2+}]^*[B_D]^{n+1}, \tag{A11}$$

where $\Delta_i = r_i - r_{i-1}$, for $i = 1$ to $I - 1$; $\Delta_j = \theta_j - \theta_{j-1}$, for $j = 1$ to J; $\Delta_k = z_k - z_{k-1}$, for $k = 1$ to $K - 1$; $r_0 = 0$; $r_I = a$; $z_0 = 0$; $z_K = \ell$; $\theta_0 = \theta_J$; $A_{ijk} = 0$ if no pumps exist, and $n_{Ca}(i, j, k) = 0$ if no Ca^{2+} channels exist. The $n_{Ca}(i, j, k)$ was varied according to whether the position located inside or outside a hotspot as well as on the bottom ($z_k = \ell$) or the surrounding membrane ($d_{Ca}\ell \le z_k < \ell$). The A_{ijk} was also specified according to whether the position was on the bottom or the surrounding membrane. The intermediate values $[Ca^{2+}]^*$, $[Ca^{2+}]^{**}$, and $[Ca^{2+}]^{n+1}$ in the denominator

of the CaATPase pump contribution to Eq. A11 are assumed to be the values of the previous iteration to transform the difference equations into a tridiagonal matrix that can be efficiently solved later (Yamada et al., 1989).

At the membrane, the difference equations of the boundary conditions can be written by introducing a fictitious compartment outside the boundaries (Smith, 1965, pp. 33–34):

$$u_{i,j,-1} = u_{i,j,1}; \quad u_{i,j,K+1} = u_{i,j,K-1}; \quad u_{I+1,j,k} = u_{I-1,j,k}. \tag{A12}$$

At these boundaries, i.e., $r_I = a$, $z_0 = 0$, and $z_K = \ell$, the $[Ca^{2+}]$ represents the averaged $[Ca^{2+}]$ over a compartment of $\Delta_I/2$ in the r direction for r_I or $\Delta_0/2$ and $\Delta_K/2$ in the z direction (Smith et al., 1996). Therefore, the terms for the CaATPase pumps and the Ca^{2+} sources in Eq. A11 should be modified at the membrane (see the implementation in Eq. A15). The innermost boundary requires a special treatment (Crank, 1975, pp. 148–149). Based on the conditions that $r/a \to 0$ and $(\partial u/\partial r)|_{r=0} = 0$, the L'Hospital's rule can be applied to give $(\partial u/\partial r)/r \approx (\partial^2 u/\partial r^2)$. Thus, a factor of 2 appears in the second-order derivative term in the r direction, whereas the first-order derivative term in the r direction and the second-order derivative term in the θ direction disappear (no angular diffusion at $r = 0$) (Smith, 1965, pp. 43–44). From the boundary condition, $(\partial u/\partial r)|_{r=0} = 0$, i.e., $u_{-1,j,k} = u_{1,j,k}$, the second-order derivative term in the r direction then can be further simplified (Smith, 1965, pp. 44–45) as follows:

$$\nabla_r^2 u_{0,j,k} = 2(a_0 + b_0)(u_{1,j,k} - u_{0,j,k}), \tag{A13}$$

where Δ_0 in the r direction is assumed as Δ_1 to calculate a_0 and b_0. The tridiagonal matrix now can be constructed. Without writing down all the tridiagonal matrices used for $[Ca^{2+}]$ and $[B_D]$ in the three alternative directions, we show the first successive $[Ca^{2+}]$ approximation as an example. The linear equations in the r direction at an arbitrary position of $\theta_0 < \theta_j < \theta_J$ and $z_0 < z_k < z_K$ are

$$\begin{aligned}
\beta_0 u_0^* + \gamma_0 u_1^* &= \lambda_0,\\
\alpha_1 u_0^* + \beta_1 u_1^* + \gamma_1 u_2^* &= \lambda_1,\\
&\vdots\\
\alpha_i u_{i-1}^* + \beta_i u_i^* + \gamma_i u_{i+1}^* &= \lambda_i,\\
&\vdots\\
\alpha_{I-1} u_{I-2}^* + \beta_{I-1} u_{I-1}^* + \gamma_{I-1} u_I^* &= \lambda_{I-1},\\
\alpha_I u_{I-1}^* + \beta_I u_I^* &= \lambda_I,
\end{aligned} \tag{A14}$$

where $i = 1$ to $I - 1$ and u represents $[Ca^{2+}]$. To avoid confusing symbols, the indices i, j, and k are substituted for r, θ, and z in the following equations. Each specific parameter then can be described in terms of the $[Ca^{2+}]$ diffusion model:

$$\beta_0 = 1/\Delta t + D_{Ca}(a_{i=0} + b_{i=0}) + k_F^+[B_F]_{0jk}^{n+1}/2 + k_D^+[B_D]_{0jk}^{n+1}/2,$$

$$\gamma_0 = -D_{Ca}(a_{i=0} + b_{i=0}),$$

$$\begin{aligned}
\lambda_0 = D_{Ca}\{&(a_{i=0} + b_{i=0})(u_{1jk}^n - u_{0jk}^n) + a_k u_{0,j,k-1}^n\\
&- (a_k + b_k)u_{0jk}^n + b_k u_{0,j,k+1}^n\} + k_F^d k_F^+([B_F^T] - [B_F]_{0jk}^{n+1})\\
&- k_F^+[B_F]_{0jk}^{n+1} u_{0jk}^n/2 + k_D^d k_D^+([B_D^T] - [B_D]_{0jk}^{n+1})\\
&- k_D^+[B_D]_{0jk}^{n+1} u_{0jk}^n/2 + u_{0jk}^n/\Delta t,
\end{aligned}$$

$$\alpha_i = \frac{-D_{Ca}}{2}\left(a_i - \frac{c_i}{r_i}\right),$$

$$\beta_i = 1/\Delta t + D_{Ca}(a_i + b_i)/2 + k_F^+[B_F]_{ijk}^{n+1}/2 + k_D^+[B_D]_{ijk}^{n+1}/2,$$

$$\gamma_i = \frac{-D_{Ca}}{2}\left(b_i + \frac{c_i}{r_i}\right),$$

$$\begin{aligned}
\lambda_i = \frac{D_{Ca}}{2}\Bigg\{&a_i u_{i-1,j,k}^n - (a_i + b_i)u_{ijk}^n + b_i u_{i+1,j,k}^n\\
&+ \frac{c_i}{r_i}(u_{i+1,j,k}^n - u_{i-1,j,k}^n) + 2[a_j u_{i,j-1,k}^n\\
&- (a_j + b_j)u_{ijk}^n + b_j u_{i,j+1,k}^n]/r_i^2 + 2[a_k u_{i,j,k-1}^n\\
&- (a_k + b_k)u_{ijk}^n + b_k u_{i,j,k+1}^n]\Bigg\} + k_F^d k_F^+([B_F^T] - [B_F]_{ijk}^{n+1})\\
&- k_F^+[B_F]_{ijk}^{n+1} u_{ijk}^n/2 + k_D^d k_D^+([B_D^T] - [B_D]_{ijk}^{n+1})\\
&- k_D^+[B_D]_{ijk}^{n+1} u_{ijk}^n/2 + u_{ijk}^n/\Delta t,
\end{aligned}$$

$$\alpha_I = -\frac{D_{Ca}}{2}(a_I + b_I),$$

$$\beta_I = 1/\Delta t + D_{Ca}(a_I + b_I)/2 + k_F^+[B_F]_{Ijk}^{n+1}/2 + k_D^+[B_D]_{Ijk}^{n+1}/2 + \frac{4\nu_{max}A_{Ijk}}{\Delta_I\Delta_j\Delta_k(4a - \Delta_I)(u_{Ijk}^n + K_m)},$$

$$\begin{aligned}
\lambda_I = \frac{D_{Ca}}{2}\Bigg\{&(a_I + b_I)(u_{I-1,j,k}^n - u_{Ijk}^n) + 2[a_j u_{I,j-1,k}^n\\
&- (a_j + b_j)u_{Ijk}^n + b_j u_{I,j+1,k}^n]/a^2 + 2[a_k u_{I,j,k-1}^n\\
&- (a_k + b_k)u_{Ijk}^n + b_k u_{I,j,k+1}^n]\Bigg\} + k_F^d k_F^+([B_F^T] - [B_F]_{Ijk}^{n+1})\\
&- k_F^+[B_F]_{Ijk}^{n+1} u_{Ijk}^n/2 + k_D^d k_D^+([B_D^T] - [B_D]_{Ijk}^{n+1})\\
&- k_D^+[B_D]_{Ijk}^{n+1} u_{Ijk}^n/2 + u_{Ijk}^n/\Delta t\\
&+ \frac{4\nu_{max}A_{Ijk}}{\Delta_I\Delta_j\Delta_k(4a - \Delta_I)}\left\{\frac{2[Ca^{2+}]_o}{[Ca^{2+}]_o + K_m}\right.\\
&\left. - \frac{u_{Ijk}^n}{u_{Ijk}^n + K_m}\right\} - \frac{4n_{Ca}(I,j,k)\bar{i}_{Ca}}{\Delta_I\Delta_j\Delta_k F(4a - \Delta_I)}.
\end{aligned} \tag{A15}$$

The equations listed above are based on the conditions that CaATPase pumps and Ca^{2+} channels are located at the membrane. Such an arrangement can easily be extended to models of other neurons that simulate intracellular processes, including Ca^{2+} uptake or release mechanisms, by assigning the values of $n_{Ca}(i, j, k)$ and A_{ijk}. As shown in Eq. A14, the set of equations in a specific direction can be rearranged as a tridiagonal matrix, which can be readily solved recursively with an efficient algorithm (Press et al., 1992, p. 51). Note that the difference equations in the θ direction are formulated as a cyclic tridiagonal matrix, which can be solved by using the Sherman-Morrison formula (Press et al., 1992, p. 75). All numerical solutions were implemented on a DEC Alphastation 200 4/233 computer. For a 10-s simulation, the averaged computation time was approximately 8 h.

REFERENCES

Art, J. J., and R. Fettiplace. 1987. Variation of membrane properties in hair cells isolated from the turtle cochlea. *J. Physiol. (Lond.)*. 385: 207–242.

Art, J. J., R. Fettiplace, and Y.-C. Wu. 1993. The effects of low calcium on the voltage-dependent conductances involved in tuning of turtle hair cells. *J. Physiol. (Lond.).* 470:109–126.

Bredderman, P. J., and R. H. Wasserman. 1974. Chemical composition, affinity for calcium, and some related properties of the vitamin D dependent calcium-binding protein. *Biochemistry.* 13:1687–1694.

Carafoli, E. 1991. Calcium pump of the plasma membrane. *Physiol. Rev.* 71:129–153.

Chad, J. E., and R. Eckert. 1984. Calcium domains associated with individual channels can account for anomalous voltage relations of Ca-dependent responses. *Biophys. J.* 45:993–999.

Crank, J. 1975. The Mathematics of Diffusion, 2nd ed. Oxford University Press, Oxford, UK.

Crawford, A. C., and R. Fettiplace. 1980. The frequency selectivity of auditory nerve fibres and hair cells in the cochlear of the turtle. *J. Physiol. (Lond.).* 306:79–125.

Crawford, A. C., and R. Fettiplace. 1981. An electrical tuning mechanism in turtle cochlear hair cells. *J. Physiol. (Lond.).* 312:377–412.

Douglas, J. 1962. Alternating direction methods for three space variables. *Numerische Mathematik.* 4:41–63.

Douglas, J., and H. H. Rachford. 1956. On the numerical solution of heat conduction problems in two and three space variables. *Trans. Am. Math. Soc.* 82:421–439.

Fettiplace, R. 1992. The role of calcium in hair cell transduction. *Soc. Gen. Physiol. Ser.* 47:343–356.

Fullmer, C. S., and R. H. Wasserman. 1987. Chicken intestinal 28-kilodalton calbindin-d: complete amino acid sequence and structural considerations. *Proc. Natl. Acad. Sci. USA.* 84:4772–4776.

Gross, M. D., M. Gosnell, A. Tsarbopoulos, and W. Hunziker. 1993. A functional and degenerate pair of EF hands contains the very high affinity calcium-binding sites of calbindin-D28k. *J. Biol. Chem.* 268: 20917–20922.

Gunter, T. E., and D. R. Pfeiffer. 1990. Mechanisms by which mitochondria transport calcium. *Am. J. Physiol.* 258: C755–C786.

Heidelberger, R., C. Heinemann, E. Neher, and G. Matthews. 1994. Calcium dependence of the rate of exocytosis in a synaptic terminal. *Nature.* 371:513–515.

Hille, B. 1992. Ionic Channels of Excitable Membranes, 2nd ed. Sinauer Associates, Sunderland, MA.

Hudspeth, A. J., and R. S. Lewis. 1988. A model for electrical resonance and frequency tuning in saccular hair cells of the bullfrog. *Rana catesbeiana. J. Physiol. (Lond.).*. 400:275–297.

Jackson, A. P., M. P. Timmerman, C. R. Bagshaw, and C. C. Ashley. 1987. The kinetics of calcium binding to fura-2 and indo-1. *FEBS Lett.* 216: 35–39.

Lenzi, D., and W. M. Roberts. 1994. Calcium signaling in hair cells: multiple roles in a compact cell. *Curr. Opin. Neurobiol.* 4:496–502.

Llinás, R. R., M. Sugimori, and R. B. Silver. 1992. Microdomains of high calcium concentration in a presynaptic terminal. *Science.* 256:677–679.

Llinás, R. R., M. Sugimori, and R. B. Silver. 1995. The concept of calcium concentration microdomains in synaptic transmission. *Neuropharmacology.* 34:1443–1451.

Mascagni, M. V. 1989. Numerical methods for neuronal modeling. *In* Methods in Neuronal Modeling: From Synapses to Networks. C. Koch and I. Segev, editors. MIT Press, Cambridge, MA. 439–484.

Neher, E. 1986. Concentration profiles of intracellular calcium in the presence of a diffusible chelator. *In* Calcium Electrogenesis and Neuronal Functioning. U. Heinemann, M. Klee, E. Neher, and W. Singer, editors. Springer, Berlin. 80–96.

Nowycky, M. C., and M. J. Pinter. 1993. Time courses of calcium and calcium-bound buffers following calcium influx in a model cell. *Biophys. J.* 64:77–91.

Oberholtzer, J. C., C. Buettiger, M. C. Summers, and F. M. Matchinsky. 1988. The 28-kDa calbindin-D is a major calcium-binding protein in the basilar papilla of the chick. *Biochemistry.* 85:3387–3390.

Oliva, C., I. S. Cohen, and R. T. Mathias. 1988. Calculation of time constants for intracellular diffusion in whole cell patch clamp configuration. *Biophys. J.* 54:791–799.

Petrozzino, J. J., L. D. Pozzo Miller, and J. A. Connor. 1995. Micromolar Ca^{2+} transients in dendritic spines of hippocampal pyramidal neurons in brain slices. *Neuron.* 14:1223–1231.

Press, W. H., S. A. Teukolsky, W. T. Vetterling, and B. R. Flannery. 1992. Numerical Recipes in C: The Art of Scientific Programming. Cambridge University Press, Cambridge, UK.

Roberts, W. M. 1994. Localization of calcium signals by a mobile calcium buffer in frog saccular hair cells. *J. Neurosci* 14:3246–3262.

Roberts, W. M., R. A. Jacobs, and A. J. Hudspeth. 1990. Colocalization of ion channels involved in frequency selectivity and synaptic transmission in presynaptic active zones of hair cells. *J. Neurosci* 10:3664–3684.

Sala, F., and A. Hernández-Cruz. 1990. Calcium diffusion modeling in a spherical neuron: relevance of buffering properties. *Biophys. J.* 57: 313–324.

Schatzmann, H. 1989. The calcium pump of the surface membrane and the SR. *Annu. Rev. Physiol.* 51:473–485.

Simon, S. M., and R. R. Llinás. 1985. Compartmentalization of the submembrane calcium activity during calcium influx and its significance in transmitter release. *Biophys. J.* 48:485–498.

Sivaramakrishnan, S., and G. Laurent. 1995. Pharmacological characterization of presynaptic calcium currents underlying glutamatergic transmission in the avian auditory brainstem. *J. Neurosci.* 15:6576–6585.

Smith, G. D. 1965. Numerical Solution of Partial Differential Equations: Finite Difference Methods. Oxford University Press, London.

Smith, G. D., J. Wagner, and J. Keizer. 1996. Validity of the rapid buffering approximation near a point source of calcium ions. *Biophys. J.* 70:2527–2539.

Sneary, M. G. 1988. Auditory receptor of the red-eared turtle. II. Afferent and efferent synapses and innervation patterns. *J. Comp. Neurol.* 276: 588–606.

Strikwerda, J. C. 1989. Finite difference schemes and partial differential equations. Wadsworth and Brooks, Pacific Grove, CA.

Timmerman, M. P., and C. C. Ashley. 1986. Fura-2 diffusion and its use as an indicator of transient free calcium changes in single striated muscle cells. *FEBS Lett.* 209:1–8.

Tse, A., F. W. Tse, and B. Hille. 1994. Calcium homeostasis in identified rat gonadotrophs. *J. Physiol.* 477:511–525.

Tsien, R. Y. 1980. New Ca^{2+} indicators and buffers with high selectivity against magnesium and protons: design, synthesis, and properties of prototype structures. *Biochemistry.* 19:2396–2404.

Tucker, T., and R. Fettiplace. 1995. Confocal imaging of calcium microdomains and calcium extrusion in turtle hair cells. *Neuron.* 15:1323–1336.

Tucker, T., and R. Fettiplace. 1996. Monitoring calcium in turtle hair cells with a calcium-activated potassium channel. *J. Physiol.* 493:613–626.

Yamada, W. M., C. Koch, and P. R. Adams. 1989. Multiple channels and calcium dynamics. *In* Methods in Neuronal Modeling: From Synapses to Networks, C. Koch and I. Segev, editors. MIT Press, Cambridge, MA. 93–133.

Yamada, W. M., and R. Zucker. 1992. Time course of transmitter release calculated from simulation of a calcium diffusion model. *Biophys. J.* 61:671–682.

Weiss, T. F., and C. Rose. 1988. A comparison of synchronization filters in different auditory receptor organs. *Hearing Res.* 33:175–180.

Wu, Y.-C., J. J. Art, M. B. Goodman, and R. Fettiplace. 1995. A kinetic description of the calcium-activated potassium channel and its application to electrical tuning of hair cells. *Prog. Biophys. Mol. Biol.* 63: 131–158.

Wu, Y.-C., and R. Fettiplace. 1996. A developmental model for generating frequency maps in the reptilian and avian cochlea. *Biophys. J.* 70: 2557–2570.